Materials Science and Engineering B 330 (2026) 119520

Contents lists available at ScienceDirect

Materials Science & Engineering B

journal homepage: www.elsevier.com/locate/mseb

POME-derived $Ag/Bi_2MoO_6/TiO_2$ ternary nanocomposite: Structural design, optical properties, and multifunctional photocatalytic performance

Devagi Kanakaraju [a,*], Danielson Ngo Joseph [a], Ying Chin Lim [b],
Khairul Anwar bin Mohamad Said [c], Micky Vincent [a], Md. Rezaur Rahman [c]

[a] Faculty of Resource Science and Technology, Universiti Malaysia Sarawak, 94300 Kota Samarahan, Sarawak, Malaysia
[b] School of Chemistry and Environment, Faculty of Applied Sciences, Universiti Teknologi MARA, 40450 Shah Alam, Selangor, Malaysia
[c] Department of Chemical Engineering and Energy Sustainability, Faculty of Engineering, Universiti Malaysia Sarawak, 94300 Kota Samarahan, Sarawak, Malaysia

ARTICLE INFO

Keywords:
Green synthesis
Microwave-assisted synthesis
Photocatalysis
Antibacterial
Membrane immobilization

ABSTRACT

The development of visible-light-responsive, multifunctional photocatalysts is critical for advancing solid-state materials for environmental and antimicrobial applications. Conventional Ag/TiO_2 photocatalytic systems offer a promising solution for visible-light responsiveness and antimicrobial properties, but often suffer from poor stability and recovery, as well as complex synthesis routes. In this work, a ternary $Ag/Bi_2MoO_6/TiO_2$ (ABMOT) heterojunction photocatalyst was synthesized via a green, microwave-assisted approach using palm oil mill effluent (POME) as a natural reducing and stabilizing agent, thereby addressing waste valorization alongside material fabrication. Structural, morphological, and optical properties were systematically investigated using FTIR, XRD, PL, XPS, TEM, SEM-EDX, and UV–Vis DRS, thereby confirming the successful formation of a heterojunction and the enhancement of visible-light absorption. The ABMOT nanocomposite achieved 97.2% degradation of oxytetracycline under visible light irradiation at an optimal dosage of 0.6 g/L, attributed to its strong adsorption capacity, pollutant tolerance, and structural stability over four successive cycles. In addition, ABMOT imparted notable antibacterial activity against *Escherichia coli* and *Staphylococcus aureus*, demonstrating its multifunctional nature. To overcome the recovery limitations of slurry photocatalysts, ABMOT was immobilized in polyacrylonitrile (PAN) membranes via the phase inversion, resulting in improved hydrophilicity, porosity, water flux, and pollutant rejection. This study presents a sustainable approach to designing multifunctional ABMOT ternary photocatalysts with enhanced optical and physicochemical properties, providing insights into circular-economy-driven solid-state materials for advanced separation and photocatalytic technologies.

1. Introduction

The global escalation of pharmaceutical contaminants, particularly antibiotics such as oxytetracycline (OTC), poses a significant threat to aquatic ecosystems and human health due to their persistence and role in promoting antibiotic-resistant bacteria [1]. Traditional wastewater treatment methods such as coagulation, flocculation, and bioremediation often fall short in completely mineralizing these persistent molecules [2–4]. Therefore, there is a need to develop improved water treatment technologies, such as advanced oxidation processes (AOPs). Among the various AOPs, heterogeneous photocatalysis has emerged as a promising tool in the complete mineralization of pollutants. This is because photocatalysis uses solar energy to generate reactive oxygen species (ROS), such as hydroxyl and superoxide radicals, that degrade organic pollutants into harmless byproducts [5].

While TiO_2 has long been a benchmark material in photocatalysis due to its non-toxicity and chemical stability, its wide bandgap (~3.2 eV) limits its activity to the UV region and leads to rapid electron-hole recombination. To overcome these limitations, the design of multifunctional ternary or binary nanocomposites (NCs) has emerged as a key research frontier in recent decades [6,7]. Specifically, integrating Bi_2MoO_6 and Ag with TiO_2 offers a synergistic solution. This is because Bi_2MoO_6 exhibits visible-light responsiveness due to its narrow bandgap (~2.5–2.9 eV) [8]. Whereas metallic Ag can act as a plasmonic sensitizer via surface plasmon resonance (SPR) and as an electron mediator [9–11]. The electronic compatibility among these three components

---

[*] Corresponding author.
E-mail address: kdevagi@unimas.my (D. Kanakaraju).

https://doi.org/10.1016/j.mseb.2026.119520
Received 18 December 2025; Received in revised form 17 April 2026; Accepted 20 April 2026

enables a *Z*-scheme heterojunction that spatially separates charge carriers while preserving the high redox potentials required for OTC degradation and antimicrobial activity [12,13].

Despite the potential of such systems, most fabrication routes rely on harsh solvent systems and toxic reducing agents. Hence, plant extracts, microorganisms, or agricultural waste can be used via green synthesis to mediate the fabrication of ternary heterostructures of $Ag/Bi_2MoO_6/TiO_2$ (ABMOT), thereby providing a greener and more benign alternative to conventional synthesis. Recent studies have demonstrated that plant-derived phytochemicals can act as effective reducing, stabilizing, and capping agents, enabling controlled formation of metal oxide and complex perovskite nanostructures with desirable physicochemical properties [14,15].

The palm oil industry is among the largest in tropical regions such as Southeast Asia and Africa. Generally, about 10% of palm produce yields oil, and the remaining 90% becomes vegetative waste such as empty fruit bunches, palm press fibers, palm kernel shells, and palm oil mill effluent (POME) [16]. These wastes contain an abundance of phytochemicals, including carotenoids, phenolics, sterols, flavonoids, and tocopherols, which have been previously studied and used in the synthesis of various nanomaterials [17–21]. While the high organic content in POME could pose environmental risks, these unused compounds could also be a promising resource for the green synthesis of nanomaterials.

Previous studies have successfully demonstrated the green synthesis of Ag nanoparticles (NPs) (AgNPs) and gold nanoparticles (AuNPs) by utilizing POME as a reducing and stabilizing agent [20,22]. While these works have greatly advanced POME-derived nanomaterials, they largely focus on individual NPs. The fabrication of more complex ternary NCs requires more nuanced methods, especially when using an unconventional green source such as POME. Despite growing interest in sustainable synthesis routes, few studies have explored the formation of ternary NCs using POME as a key component. Furthermore, no comprehensive studies have investigated the photocatalytic and functional performance of POME-derived ternary systems. However, given that past studies have employed green synthesis to form multiple semiconductor heterojunctions, such as perovskite/metal oxide-based systems, the formation of complex ternary heterostructures via the POME-derived route is theoretically possible despite the complex composition of POME [23,24].

Another drawback that needs to be addressed in the application of NCs in photocatalytic treatment is the difficulty of separating their powder post-treatment. One way to overcome this drawback is to immobilize the NC on materials that are easily removed or replaced, which has recently attracted research interest in integrating photocatalytic NCs with polymeric membranes [25]. Among various membranes, polyacrylonitrile (PAN) is a well-known commercial polymer with good solubility in organic solvents, unique chemical and thermal properties, radiation stability, and low cost. However, PAN-based membranes also have disadvantages, including low chemical stability, fouling, and hydrophobicity. To enhance its properties and address its shortcomings, PAN can be modified with nanomaterials.

Therefore, this work focuses on developing a POME-derived microwave-assisted ternary ABMOT heterojunction with multifunctional performance. The key contribution of this study is the demonstration of the feasibility of valorizing POME for the synthesis of complex ternary NC systems. Additionally, the antimicrobial efficacy of the ABMOT system against *E. coli* and *S. aureus* was investigated. Finally, a proof-of-concept study investigating the compatibility of ternary ABMOT with a complex PAN matrix via phase inversion was also conducted. Overall, this study highlights the comprehensive assessment of a sustainable, multifunctional platform for advanced water remediation.

2. Experimental

2.1. Materials

For this study, starting materials titanium butoxide, $Ti(OCH_2CH_2CH_2CH_3)_4$ (97% reagent grade), bismuth (III) nitrate pentahydrate, $Bi(NO_3)_3{\cdot}5H_2O$ (ACS reagent, ≥98.0%), Sodium molybdate dihydrate, $Na_2MoO_4{\cdot}2H_2O$ (ACS reagent, ≥99%), urea, NH_2CONH_2 (ACS reagent, 99.0–100.5%), and polyvinylpyrrolidone, $(C_6H_9NO)_n$ (average $M_w \sim 1{,}300{,}000$) were purchased from Sigma-Aldrich. Hydrochloric acid (HCl), sodium hydroxide (NaOH), ethylene glycol ($HOCH_2CH_2OH$, ≥99.5%), and absolute ethanol were obtained from Merck. Silver nitrate, $AgNO_3$ (AR, 99.98%), was procured from Bendosen. Other materials include polyacrylonitrile $(C_3H_3N)_n$ (average $M_w \sim 150{,}000$), ultrapure water, UPW (HPLC grade), and dimethyl sulfoxide $(CH_3)_2SO$ (AR, ≥99.9%), which were purchased from Shanghai Macklin Biochemical Co., Ltd., Fisher Chemical, and RCI Labscan Ltd., respectively.

2.2. Preparation and evaluation of POME extract

The preparation of POME extract was carried out in accordance with the previous work of Gan et al. [20]. Raw POME was obtained from SALCRA Oil Palm Mill in Kota Samarahan, Sarawak, Malaysia, and dried at 60 °C for 24 h in a glass container. After the POME samples were dried, they were scraped and ground into a powder, then sieved to remove coarse particles. Extraction of bioactive compounds from dried POME was performed by adding a fixed amount of dried POME powder to 100 mL of distilled water, followed by stirring at 80 °C for 30 min. The mixture was then filtered using Whatman filter paper to attain the POME extract. The extract was then kept at 4 °C in a refrigerator until further use.

2.3. Preparation of TiO_2 and Bi_2MoO_6 precursors

TiO_2 was synthesized via the sol-gel method using titanium(IV) butoxide as the precursor, as previously reported in our study [26]. The sol-gel synthesis of TiO_2 was carried out by combining titanium (IV) butoxide with ethanol in a 1:2 ratio. The mixture was stirred for 30 min, then 100 mL of distilled water was added dropwise. The resulting solution was subsequently stirred for 2 h, then filtered and washed three times with distilled water and ethanol. The sol-gel was then dried at 110 °C for 2 h, followed by calcination in a furnace (Protherm PLF 110/30) at 300 °C for 5 h.

Bi_2MoO_6 was synthesized via a green solvothermal method as described in previous studies with some modifications [27,28]. In this method, 2 mmol of $Bi(NO_3)_3{\cdot}5H_2O$ and 1 mmol of $Na_2MoO_4{\cdot}2H_2O$ were each dissolved in 30 mL of ethylene glycol under magnetic stirring to produce Solutions A and B, respectively. Solutions A and B were then combined, followed by the addition of 30 mL of EtOH and a fixed amount of POME extract. The solution was then transferred into a hydrothermal reactor and kept at 150 °C for 12 h. After the reaction was complete, the precipitate was filtered and washed several times with deionized water and ethanol.The precipitate was subsequently dried at 80 °C for 12 h.

2.4. Synthesis of ternary $Ag/Bi_2MoO_6/TiO_2$

The synthesis of $Ag/Bi_2MoO_6/TiO_2$ (ABMOT) NC was performed by mixing TiO_2 and Bi_2MoO_6 at a predetermined ratio (1:0.3) in 50 mL of distilled water under controlled aqueous conditions. The mixture was stirred for 30 min. Next, Ag was deposited by mixing $AgNO_3$ with 50 mL of water, then adding POME extract. The mass of $AgNO_3$ that was added is 10% wt relative to the total TiO_2/Bi_2MoO_6 binary mass. This mixture was then added to the Bi_2MoO_6/TiO_2 mixture, followed by microwave irradiation in a commercial microwave oven at 100 W for 6 min to promote AgNP deposition. Finally, the mixture was magnetically stirred for another 2 h, then filtered, washed, dried at 80 °C for 12 h, and stored for further testing. A summary of the entire synthesis process is illustrated in Fig. 1. The specific composition of the ternary NC was determined through a series of optimization experiments (Fig. S1), in which the ratios were varied to maximize the photocatalytic degradation of OTC. A summary of the composition and respective photodegradation rates of OTC is also summarized in Table S1.

2.5. *Characterization of NCs*

Scanning electron microscopy (SEM) (Model: JEOL, JSM-IT500HR) was used to determine the morphological properties of the NCs. This was followed by an analysis of the particle size distribution of the NC using ImageJ software. The microstructural characteristics were examined using a (Model: FEI Tecnai G2 F20) transmission electron microscope (TEM) at an accelerating voltage of 200 kV. Analysis of functional groups in the NCs was performed using Fourier transform infrared spectroscopy (FTIR) (Model: Shimadzu Iraffinity-1) with KBr pellets as the standard in the wavelength range of 4000–400 cm^{-1}. X-ray diffraction (XRD, PANalytical X'pert PRO) was conducted to determine the crystalline structure and phase of the green-synthesized samples. UV–vis diffuse reflectance spectroscopy (UV–Vis DRS) (Model Carry 5000) was employed to determine the effective absorption spectra of NCs, and the Kubelka-Munk plot was established to confirm any changes in the energy bandgap. The photoluminescence (PL) emission spectra of the photocatalysts were recorded using a fluorescence spectrophotometer (PerkinElmer LS55) equipped with a xenon lamp, with an excitation wavelength of 315 nm. The valence states of the surface elements present were identified using X-ray photoelectron spectroscopy (XPS) (Model: Kratos, AXIS Ultra DLD), equipped with a monochromatic Al kα source (1486.6 eV) operated at 9 mA and 12 kV under ultra-high vacuum.

2.6. *Photocatalytic activity evaluation of ABMOT*

The photocatalytic efficiency of the synthesized NCs was determined by measuring their ability to degrade OTC antibiotics under illumination by a 300 W Xenon Lamp. To ensure visible light irradiation, a glass cutoff filter was used to block wavelengths below 420 nm. First, a fixed amount of the ternary NC was added to the 10 mg/L OTC solution, and the mixture was stirred using a magnetic stirrer. The suspension was left to stir in the dark for 1 h to allow the adsorption-desorption equilibrium of OTC on the photocatalyst to reach. After 1 h, the suspension was irradiated under visible light (300 W). The photocatalytic degradation experiment was extended for another 2 h. A fixed aliquot was taken every 30 min over the 3-h photocatalytic experiment. All aliquots of the suspension were spun with a tabletop centrifuge (Hettich, EBA 200) at 6000 rpm for 10 min before being subjected to analysis with a UV–Vis spectrophotometer. The analysis was performed by monitoring changes in the λ max at 352 nm. The removal efficiency was calculated as shown in Eq. (1):

$$\textit{Removal efficiency}\ (\%) = \frac{C_i - C_f}{C_i} \times 100\% \tag{1}$$

where C_i is the initial concentration of OTC and C_f is the final concentration of OTC. The photocatalytic treatment was conducted by varying the catalyst dosage (0.3 g/L, 0.6 g/L, 1.2 g/L) and initial concentration (10 mg/L, 15 mg/L, 20 mg/L).

To investigate the primary reactive oxygen species (ROS) involved in the photocatalytic mechanism, radical scavenger experiments were conducted by adding MeOH (0.2 mmol/L), H_2O_2 (0.2 mmol/L), and p-benzoquinone (p-bzq) (0.2 mmol/L) to the prepared OTC solution (10 mg/L) to target hydroxyl radicals, holes (h^+), and superoxide radicals, respectively. In each run, the ABMOT NC was added at the optimized dosage of 0.6 g/L. Photocatalytic experiments were carried out in a manner similar to the photocatalytic evaluation method. Each aliquot was analyzed every 30 min using a UV–Vis spectrometer at 352 nm.

2.7. *Recyclability and stability of ABMOT NC*

To evaluate the long-term performance of ABMOT ternary NC, a recyclability study was conducted to assess its stability over 4 consecutive cycles. This was achieved by conducting photocatalysis under optimized conditions: a catalyst dosage of 0.6 g/L and an initial OTC concentration of 10 mg/L. After one cycle, the photocatalyst was recovered by centrifugation, washed with distilled water and ethanol to remove residual pollutants, then dried and reused under the same experimental conditions. The aliquots from each cycle were collected as described in the method for photocatalytic activity evaluation and analyzed with a UV–Vis spectrophotometer.

Additionally, Ag leaching was also conducted on each recycled NC. To monitor potential Ag leaching and functional stability, the retrieved NC samples from each cycle were subjected to antibacterial testing via disc diffusion assay against *E. coli* and *S. aureus*. This secondary assessment used the retrieved samples at a 1 g/L concentration in PBS to verify whether the loss of Ag species occurred during degradation cycles, thereby impacting the inherent antimicrobial potency of the ternary systems.

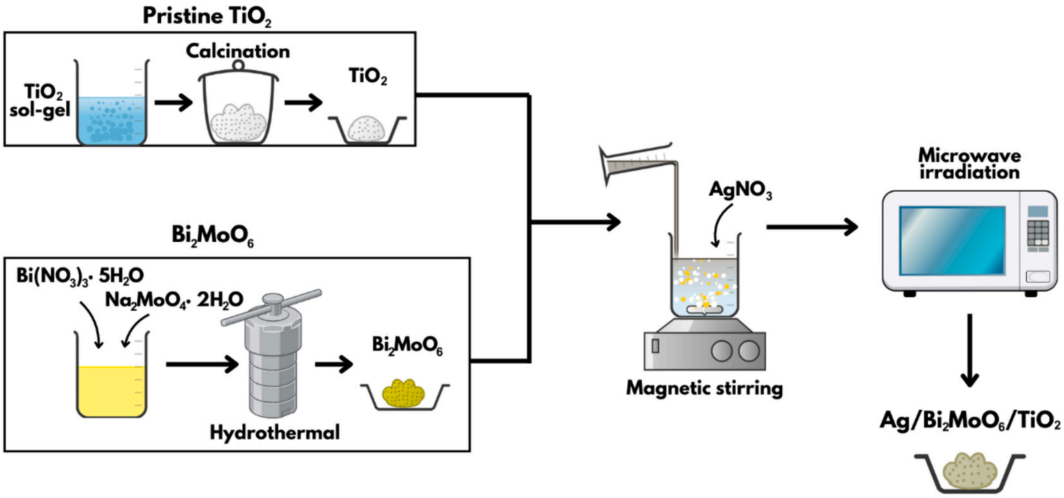

Fig. 1. Schematic illustration of $Ag/Bi_2MoO_6/TiO_2$ NC synthesis.

Next, the stability of ABMOT ternary NC in different environmental conditions was tested by substituting distilled water with river and lake water samples that were collected from the Sarawak River (1.560562°, 110.34578°) and UNIMAS Lake (1.469601°, 110.434734°), respectively. Each water matrix was spiked with 10 mg/L of OTC and treated with 0.6 g/L of catalyst. Photocatalytic experiments were conducted under identical, optimized conditions to evaluate the performance of ABMOT across different water matrices, in line with previous studies [29]. Furthermore, COD analysis was also conducted to determine the mineralization rate of OTC in different water matrices using ABMOT. The Closed Reflux Colorimetric Method, as specified in the Standard Method for Water and Wastewater Examination [30], was applied.

2.8. *Antibacterial activity evaluation*

The antibacterial study was conducted using the disc diffusion method to assess the antibacterial activity of ABMOT against Gram-positive (*E. coli*) and Gram-negative (*S. aureus*) bacteria. The bacterial strains were obtained from the Microbiology Laboratory 2 at the Faculty of Resource Science and Technology, UNIMAS. The bacterial strains were revived in nutrient broth (NB) and inoculated onto nutrient agar (NA) plates. Next, the inoculum was standardized by transferring several colonies into fresh NB and adjusting the culture to a turbidity equivalent to a 0.5 McFarland standard. The antibacterial assay was conducted by first comparing the effectiveness of ABMOT against its unary and binary counterparts in inhibiting bacterial growth. All samples were fixed at a concentration of 1 g/L. A determined amount of the mentioned samples was mixed with phosphate-buffered saline (PBS) solution. Sterile filter papers were then dipped into the PBS solution containing these samples. Following this, the standardized inoculum was swabbed onto NA plates with sterile cotton swabs, and the treated filter papers were placed on the agar surface and incubated at 37 °C for 24 h. The diameter of the inhibition zones was measured after the incubation period. This experiment was repeated by varying the ABMOT concentration to 1, 2, 4, 8, and 10 g/L.

2.9. *Application of biosynthesized NCs with PAN membrane*

2.9.1. *Preparation of $Ag/Bi_2MoO_6/TiO_2$@PAN membrane*

The fabrication of NCs into the PAN membrane was carried out using the phase inversion method. In this process, 85 g of DMSO was measured and poured into a beaker. This was followed by the addition of 1% of ABMOT NC based on the weight of PAN into the beaker containing the solvent. The solution was stirred at 80 °C for 1 h. After thorough mixing, the solution was transferred into a conical flask, where 15 g of PAN powder was added. The mixture was then continuously stirred at 80 °C for 24 h until complete dissolution and homogenization were achieved. After the casting solution was fully dissolved and homogenized, it was sonicated for 10 min to remove any entrapped air bubbles prior to casting. The final solution was then hand-cast onto a clean glass plate using a metal rod to obtain a uniform membrane film. To ensure uniform and precise film thickness, adhesive tapes with a thickness of 100 µm were applied to the longitudinal edges of the glass plates to serve as a spacer. The glass plate was then immersed in a coagulation bath to induce phase inversion, forming a solid membrane. After complete phase separation, the membrane was carefully peeled off and further soaked in ultrapure water to remove residual solvents. The final membranes were stored in ultrapure water until further use. A bare PAN membrane was also prepared in the same manner, without NC. The NC loading percentages were strategically selected with reference to a prior study as representative benchmarks for evaluating the structural and chemical compatibility of the ABMOT ternary NC within the PAN matrix [31,32]. This serves as a proof of concept for the immobilization of complex ternary NCs within a polymer support. The composition used to prepare the bare PAN membrane and NC membranes is summarized in Table 1.

Table 1
Composition of ABMOT NC-embedded PAN membranes.

Membrane	PAN (g)	DMSO (g)	NC loading (g)
PAN	15.00	85.00	0.00
1% ABMOT@PAN	15.00	85.00	0.15
2% ABMOT@PAN	15.00	85.00	0.30

2.9.2. *Characterization of the synthesized membrane*

The characterization of the membranes was performed using SEM coupled with EDX to determine their surface morphology and cross-section. Additionally, FTIR analysis was conducted to confirm the chemical interaction of NCs within the membrane matrix via FTIR spectroscopy (Model: Thermo Nicolet iS10), equipped with attenuated total reflectance (ATR), in the spectral range of 2000–400 cm^{-1}. Moreover, the water contact angle (WCA) of the membrane samples was measured using a goniometer (Model: OSSILA L2004A1) to assess the hydrophilicity of the NC-modified membranes. Finally, the porosity of the NC membranes and pristine membranes was also calculated using the gravimetric method, based on the weight of water in the membrane pores, as in a previous study by Tavakolmoghadam et al. [33]. The equation for the calculation of the membrane porosity was done as follows:

$$\varepsilon = \frac{\left(\frac{w_{wet\ membrane} - w_{dry\ membrane}}{\rho_{water}}\right)}{\left(\frac{w_{wet\ membrane} - w_{dry\ membrane}}{\rho_{water}}\right) + \left(\frac{w_{dry\ membrane}}{\rho_{PAN}}\right)} \times 100\ (\%) \tag{2}$$

where ε refers to the membrane porosity, $w_{wet\ membrane}$, is the weight of the wet membrane, $w_{dry\ membrane}$ is the weight of the dry membrane, ρ_{water} is the density of water (0.998 $g.cm^{-3}$), and $\rho_{PAN}$is the density of PAN (1.184 $g.mL^{-1}$).

2.9.3. *Evaluation of membrane filtration properties*

The membrane permeation test served as the primary evaluation to compare the performance of pristine PAN membranes with that of membranes incorporated with ABMOT ternary NC. This test consisted of pure water flux and OTC rejection. For the pure water flux test, membranes were compacted using a backflow that was recirculated into the filtration system feed. Pure water flux was determined by pumping ultrapure water into the system at 2 bar for 1 h to stabilize the membrane system. Then, the water flux test was conducted at 1 bar for another hour, with results recorded every 10 min. The procedure was repeated 3 times to ensure accurate reading and replicability of water flux results. Similarly, the OTC rejection test was performed using the same procedure, with 10 g/L OTC solution as the feed. The concentrations of the initial feed and permeate were measured using a UV–Vis spectrophotometer (Model: Perkin-Elmer LS55) at a λ max of 352 nm. The water flux and OTC rejection were obtained following the equation as described by Huang et al. [34]:

$$J_{flux} = \frac{V}{A \times t \times P}\ \left(L{\cdot}m^{-2}{\cdot}h^{-1}\right) \tag{3}$$

$$RR\ (\%) = \frac{C_{feed} - C_{permeate}}{C_{feed}} \times 100\% \tag{4}$$

where, J_{flux} represents the water flux ($L{\cdot}m^{-2}{\cdot}h^{-1}$), V is the volume of permeate, A, is the effective area of membrane (m^2), P is the operational pressure (bar), RR is rejection rate (%), C_{feed} is the concentration of OTC in the feed and $C_{permeate}$ is the concentration of OTC from the permeate collected.

3. Results and discussion

3.1. *Characterization of Ag/Bi_2MoO_6/TiO_2*

3.1.1. *Morphological and structural analysis*

Fig. 2a shows the FTIR spectrum of ABMOT, compared with those of its individual counterparts. FTIR analysis shows that pristine TiO_2 had broad absorption peaks at ~3100–3600 cm^{-1} and strong peaks at 640 cm^{-1} corresponding to -OH stretching and Ti-O-Ti bonds, respectively. Bi_2MoO_6, on the other hand, showed strong characteristic peaks at 1107 cm,$^{-1}$ 813 cm,$^{-1}$ and 729 cm^{-1}, Bi—O bond, Mo—O stretching vibration modes, and MoO_6 asymmetric stretching, respectively [35,36]. AgNPs characteristic bands at 1384 and 1620 cm^{-1} are mainly ascribed to C═C stretching of aliphatic alkenes and C═O from aldehydes or ketones, respectively [37]. Peaks at around 671 and 779 cm^{-1} indicate Ag-O-Ag stretching modes [38]. In the case of ABMOT, most of the characteristic bands of TiO_2 were maintained, except for the appearance of broader bands between 600 and 800 cm,$^{-1}$ a distinct peak at 1384 cm^{-1}, and a widened peak at 3142 cm.$^{-1}$ The observed could be linked to the presence of Bi—O and Mi-O bonds and bound organic compounds as

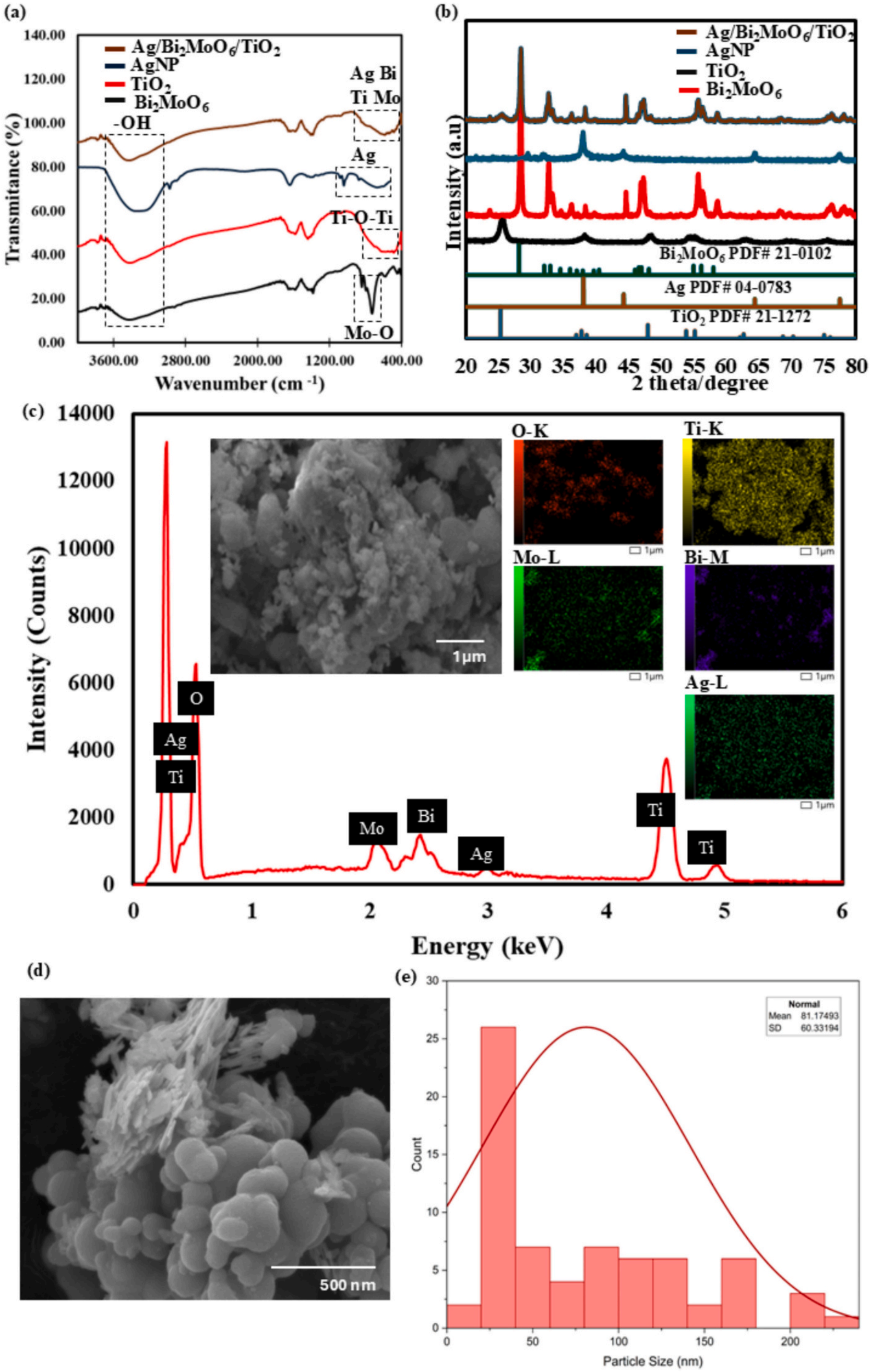

Fig. 2. (a) FTIR and (b) XRD spectra of ABMOT, AgNP, TiO_2, and Bi_2MoO_6, (c) EDX spectra and elemental mapping of ABMOT, (d) SEM image of ABMOT (60,000× magnification), and (d) particle size distribution of ABMOT NCs.

described.Thus, the FTIR spectra of the samples confirm the presence of all key functional groups associated with ABMOT ternary heterostructures.

Further characterization by XRD was conducted to investigate the crystalline structure and phase composition of the synthesized samples (Fig. 2b). The diffraction patterns were compared with Joint Committee on Powder Diffraction Standards (JCPDS) standards to identify characteristic peaks for each phase. It can be observed that pristine TiO_2 showed characteristic $2\theta = 25.4°$, $38.5°$, $48.1°$, $55.1°$, $63.0°$ (JCPDS 21–1272) corresponding to anatase phase (101), (004), (200), (211), (204), and (220) crystal faces, respectively. The anatase phase of TiO_2 is well known for its highest photocatalytic activity among the polymorphs [39]. This makes it suitable for combining with other materials to further enhance its properties. Given the dominant formation of (101) crystal facets, the synthesized TiO_2 is thermodynamically stable, which is favorable for long-term structural stability [40]. On the other hand, individual samples of AgNPs exhibited peaks of Ag (200) at $2\theta = 44.6°$, Ag (220) and $2\theta = 64.6°$, and Ag (311) at $2\theta = 77.4°$ (JCPDS 04–0783) (Fig. 2b). Similar peaks were observed in a past study by Aleiro et al. [22] in which the characteristic peaks of AgNPs that were synthesized with POME also exhibited peaks corresponding to (200), (220), and (311). However, the major peaks at $2\theta = 28°$, $32°$, and $38°$ were absent in the POME-derived AgNPs of this study, suggesting the macromolecular phytoconstituents and bioactive compounds from POME were not present on the NP surface [41]. This absence could be due to the drying process, which likely removed these phytoconstituents from the surface of the synthesized AgNPs. The diffraction peaks of pure Bi_2MoO_6 showed distinctive peaks around $2\theta = 28.3°$, $32.5°$, $47.1°$, and $55.8°$ corresponding to (131), (200), (260) and (331) planes, respectively (Fig. 2b). The XRD pattern suggests the formation of the orthorhombic Aurivillius phase of γ- Bi_2MoO_6 (JCPDS 21–0102), thus confirming the succession of crystalline Bi_2MoO_6. This phase is desirable as it has a greater capacity to capture visible light than its fluorite-structured counterparts, α-$Bi_2Mo_3O_{12}$ and β-$Bi_2Mo_2O_9$ [42]. Upon the formation of ternary ABMOT NC, Ag peaks at $2\theta = 44.6°$ (200) and $2\theta = 64.8°$ (220) were detected, confirming that AgNPs were successfully deposited into the ternary NC matrix (Fig. 2b). Similarly, all characteristic peaks of Bi_2MoO_6 and TiO_2 were retained, albeit with reduced intensity. This indicates the coexistence of the different phases within the ternary components and reflects increased structural distortion, a typical feature in most NC systems.

Moreover, photocatalytic performance is often linked to their morphology [43]. Therefore, further morphological and elemental characterization was performed using SEM-EDX. The surface morphology of pristine TiO_2 synthesized via the sol-gel method exhibits smooth, spherical NPs that tend to agglomerate (Fig. S2a), a common feature in nano-TiO_2 due to its high surface energy, van der Waals forces, and hydrogen bonding, which drive the NPs to cluster together [44,45]. Similarly, POME-derived AgNPs also formed spherical aggregates (Fig. S2b). Similar results were also reported by Gan et al. [20], who observed spherical POME-derived AuNPs with uniformly distributed aggregates. More recently, another study reported that POME-derived AgNPs exhibited evenly distributed spherical NPs stabilized by specific bioactive compounds such as ascorbic acid, gallic acid, and vanillic acid, thereby facilitating controlled particle size and shape [46]. On the contrary, Bi_2MoO_6 formed very distinctive morphologies. Bi_2MoO_6 exhibited nanoplate-like structures that overlapped (Fig. S2c). A similar morphology of green hydrothermally synthesized perovskite Bi_2WO_6 was also observed by Kanwal et al. [27]. In their study, the perovskite nanomaterial was synthesized using *Azadirachta indica* leaves, which facilitated controlled nucleation and prevented uncontrolled aggregation of the growing crystallites, thereby allowing the formation of plate-like nanostructures that aggregate into a flower-like aggregate [27]. The ternary composites appeared more compact and homogeneous, suggesting successful assembly of the components via microwave-assisted routes (Fig. 2c). This method provides a favorable environment for the uniform dispersion and anchoring of the components through direct interactions with polar molecules [47]. This enables an even removal of dispersants and allows for consistent nucleation throughout the system [48]. Additionally, elemental mapping via EDX (Fig. 2c) confirms the uniform distribution of each component, with ratios of Ti, Ag, Bi, Mo, and O of 52.00%, 2.97%, 10.87%, 3.93%, and 30.23%, respectively (Table 2). This data supports the XRD findings of successful material integration. Nevertheless, it is worth noting that the overall composition and distribution of elements may not directly translate to the mass percentages of elements detected by EDX mapping, as different elements may be preferentially adsorbed at the surface within the ternary matrix [49]. To further elucidate the nanoscale characteristics of the ABMOT ternary NC, a higher-resolution image and the corresponding particle size distribution were analyzed (Fig. 2d and e). The particle sizes of the ternary NC were measured manually in ImageJ using the SEM image scale, with a total of 70 measurements. The particles predominantly fall within the nanometer range, with an average particle size of ~81.17 nm and a standard deviation of ±60.33 nm. The relatively large standard deviation reflects the heterogeneous nature of the ternary composites, in which a mixture of smaller NPs, larger agglomerates, and irregularly shaped structures contributed to a broader distribution of the particle sizes as observed in Fig. 2d. This variability is a common characteristic of a multicomponent NC and further supports the successful integration of the different constituents within the ternary NC. Despite POME acting as a reducing and stabilizing agent, it may not fully prevent post-synthesis aggregation during drying and calcination. In fact, such hierarchical aggregations might even be beneficial, as they increase light scattering, which could improve photocatalytic performance [50].

Additionally, the nanoscale structure and interfacial characteristics of the ABMOT ternary NC were analyzed with HRTEM (Fig. 3). The TEM images (Fig. 3a) clearly reveal the hierarchical structure of the composite, where Bi_2MoO_6 nanoplates appear to serve as the primary substrate for the uniform dispersion of TiO_2 and Ag NPs. HRTEM revealed well-defined lattice fringes, which confirms the crystalline nature of the composite (Fig. 3b). Two prominent interplanar spacings of approximately 0.335 nm and 0.229 nm were observed. The lattice spacing of 0.335 nm can be attributed to the (140) crystal plane of orthorhombic Bi_2MoO_6, which is consistent with previous reports [51]. Consequently, the spacing of 0.229 nm corresponds to the (111) plane of metallic Ag. This is further supported by the appearance of darker contrast regions, which are due to their higher atomic number [52]. Notably, lattice fringes corresponding to anatase TiO_2 (101), which are usually ~0.350 nm, were not distinctly observed in the selected regions. This may be caused by the high dispersion of TiO_2, the dominant component of the NC coating, and the Bi_2MoO_6 nanoplates, leading to lattice signal overlap or a preferential orientation that favors the visibility of the (140) planes [51]. Moreover, the corresponding selected area electron diffraction (SAED) pattern exhibited a series of concentric diffraction rings with discrete bright spots (Fig. 3c). This indicates that ABMOT NCs possess a polycrystalline structure. These diffraction rings can be attributed to the overlap of individual components in the ternary NC, as is commonly reported in the literature [52,53]. The spotty nature of the rings further suggests the presence of nanocrystalline domains with random orientations, providing a high density of active sites for photocatalytic reactions. The overall observations in the HRTEM and SAED images are consistent with the crystalline phases identified in the XRD

Table 2
Elemental composition of ABMOT NC.

Elements	Mass (%)
Ti	52.00 ± 0.26
O	30.23 ± 0.13
Ag	2.97 ± 0.08
Bi	10.87 ± 0.16
Mo	3.93 ± 0.08

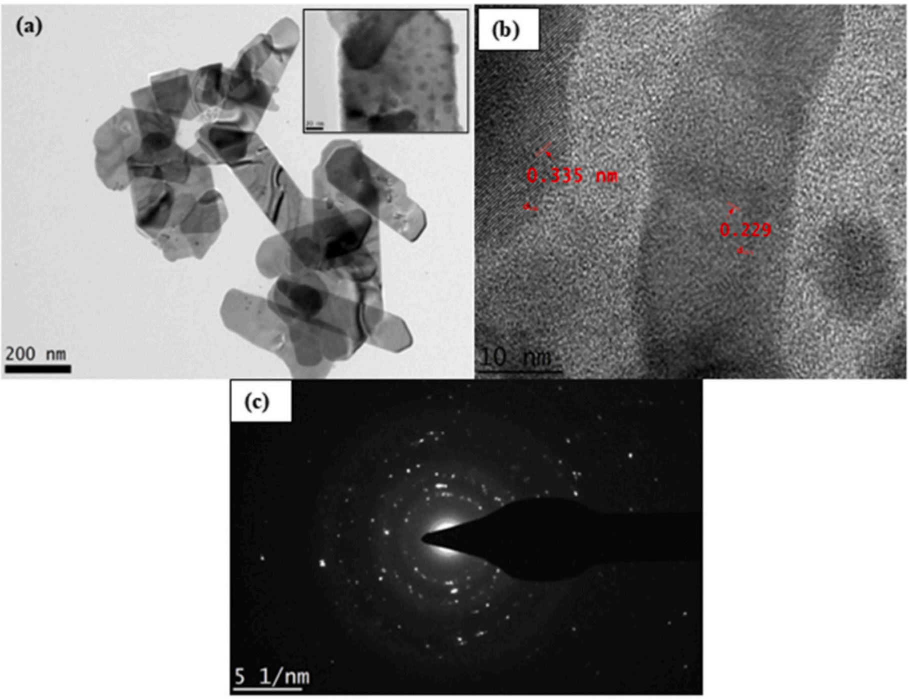

Fig. 3. (a) TEM images of ABMOT, (b-c) HRTEM images of ABMOT, and (d) SAED image of ABMOT.

analysis.

The surface elemental composition and chemical states of the green synthesized ABMOT ternary NC were investigated using XPS. As shown in the survey scan (Fig. 4a), the characteristic peaks of Bi 4f, Mo 3d, Ti 2p, Ag 3d, and O 1 s are clearly identified. This confirms the successful integration of all three components of TiO_2, Bi_2MoO_6, and AgNPs within the heterojunction, thus supporting claims from characterizations via EDX, XRD, and FTIR. To further identify the chemical states of each element, high-resolution XPS spectra were recorded for each (Fig. 4b-f). As shown in Fig. 4b, the O 1 s peaks are deconvoluted into two prominent peaks, which correspond to lattice oxygen (O_l) peaks from Mo—O at 528.1 eV and oxygen vacancy (O_v) peaks from Ti-O-Ti/Bi-O peaks at 529.8 eV. This observation is consistent with findings from previous studies [51]. The presence of O_v, resulting from the interaction between TiO_2 and Bi_2MoO_6, indicates a higher electron density, which is beneficial as it can serve as electron traps that facilitate efficient charge separation [52]. The Ti 2p spectrum (Fig. 4c) displays dominant peaks at 458.8 eV and 464.4 eV, corresponding to Ti $2p_{3/2}$ and Ti $2p_{1/2}$ states of Ti^{4+} in the TiO_2 lattice [53]. Interestingly, the slightly deconvoluted shoulders at lower binding energies at 456.9 eV and 462.8 eV indicate the presence of Ti^{3+} species. The existence of Ti^{3+} is inherently linked to the formation of oxygen vacancies as observed in O 1 s spectra [52]. Similarly to TiO_2, peaks of Bi 4f (Fig. 4d) show the position of Bi $4f_{7/2}$ (157.9 eV) and Bi $4f_{5/2}$ (163.2 eV) corresponding to Bi^{3+} within the Bi_2MoO_6 lattice [51]. The deconvoluted peaks at lower energies are attributed to Bi^{3+} surface species in a more electron-rich environment near the heterojunction interface, possibly due to interactions with Ag [54]. Unlike the sharp doublets observed in Bi 4f and Ti 2p, the Mo 3d spectrum (Fig. 4e) appears as a broad, complex envelope. This lack of prominent peak splitting can be attributed to multiple oxidation states and significant electronic perturbations at the heterojunction interface. While the peaks at 232.5 eV and 235.6 eV correspond to the standard $3d_{5/2}$ and $3d_{3/2}$ states of Mo^{6+} in Bi_2MoO_6, the spectrum is heavily influenced by a prominent deconvoluted peak at 230.9 eV,

which is induced by the strong interactions between Bi_2MoO_6 and Ag [55]. Moreover, the peaks of Ag 3d at 368.1 eV and 374.1 eV (Fig. 4f) suggest the dominant presence of metallic Ag^0. In the ternary system, Ag acts as a strong electronic mediator, thus transferring electron density towards the Mo centers. This accumulation of charge causes Mo 3d binding energies to shift and overlap, masking the traditional clean doublet splitting of Mo^{6+} states [55]. Therefore, the aforementioned characterizations confirm the successful green synthesis of the ternary ABMOT comprising TiO_2, Bi_2MoO_6, and AgNPs.

3.1.2. Optoelectrical properties

Optical properties of TiO_2, Bi_2MoO_6, Bi_2MoO_6/TiO_2, and ABMOT were determined through UV-DRS analysis as depicted in Fig. 5a and b. Bandgap values were determined via the Tauc plot method [51]. The following equation was employed:

$$(ahv)^{1/n} = A\left(hv - E_g\right) \tag{5}$$

where hv is the photon energy, A is the proportionality constant, E_g refers to the energy bandgap, a refers to the absorption factor, and n is the transition-specific exponent, where $n = 2$ for indirect allowed transitions and $n = 1/2$ for direct allowed transitions. In this case, both TiO_2 and Bi_2MoO_6 are treated as direct allowed transitions in the plot of $(ahv)^{1/n}$ against hv to determine their respective apparent bandgap energies, as reported in the literature [56].

Pure TiO_2 showed a sharp absorption edge at around 400 nm with a bandgap of 3.00 eV, confirming that it mainly absorbs UV light. In contrast, Bi_2MoO_6 exhibited a broader absorption up to about 470 nm and a narrower bandgap of 2.60 eV, consistent with its known ability to absorb visible light. The Bi_2MoO_6/TiO_2 binary composite displayed improved absorption between 300 and 450 nm, indicating effective heterojunction formation that enhances charge separation and broadens the absorption spectrum. Notably, the $Ag/Bi_2MoO_6/TiO_2$ NC exhibited the highest absorption intensity, with a broad band extending beyond 500 nm. This improvement is mainly due to the localized SPR effect of AgNPs, which strengthens local electromagnetic fields and extends light absorption into the visible range [51,57]. Additionally, the contact between AgNPs and TiO_2, as well as Bi_2MoO_6, facilitates the formation of Schottky junctions. Overall, the composites exhibit extended visible light absorption rather than a well-defined bandgap transition.

These optical properties provided insight into the electronic transition within the ABMOT heterojunction. The bandgap narrowing and the

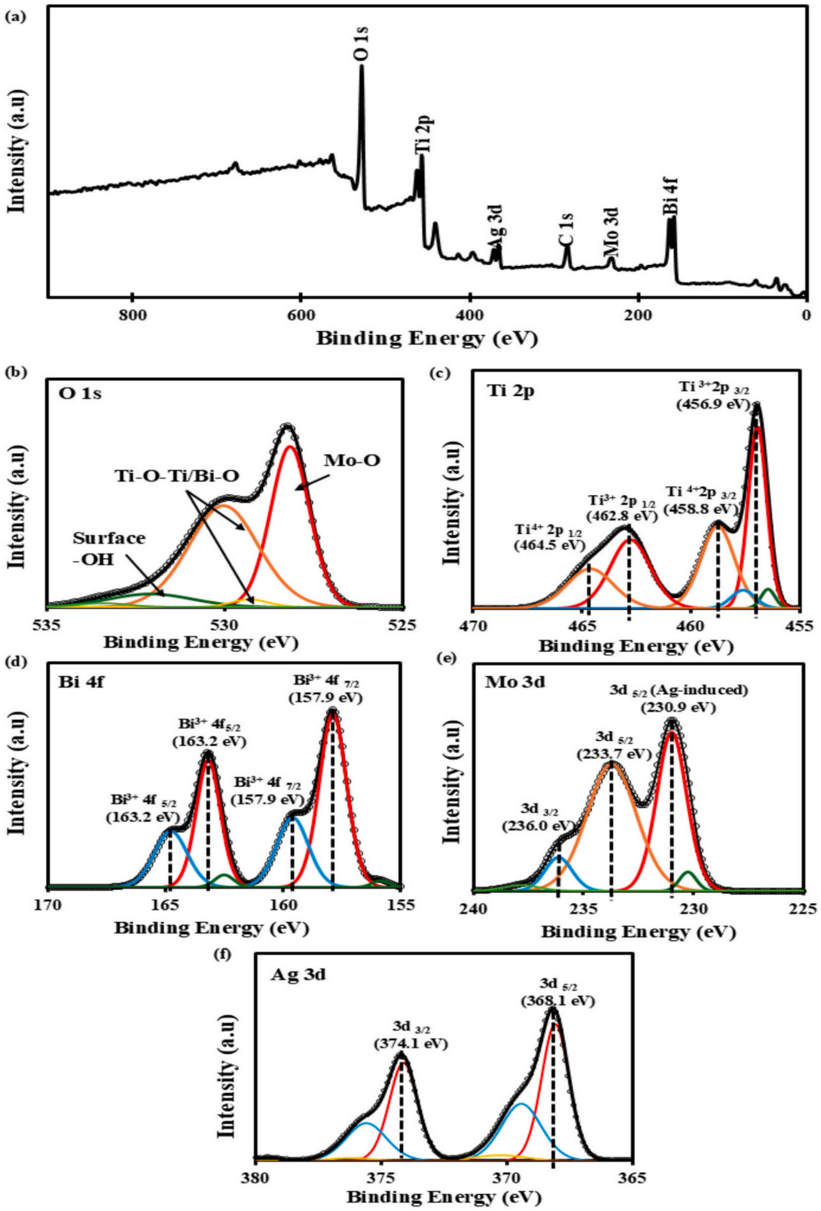

Fig. 4. (a) XPS survey spectrum of ABMOT NC and high-resolution XPS spectra of (b) O 1 s, (c) Ti 2p, (d) Bi 4f, (e) Mo 3d, and (f) Ag 3d.

increase in visible light absorption indicate a synergistic interaction among the three components of the NC. Given the work function of Ag, which is roughly 4.26 eV and lower than the conduction band (CB) levels of TiO_2 and Bi_2MoO_6, a potential barrier forms at the interface [58]. This Schottky barrier acts as a directional sink for excited electrons, trapping them on the Ag surface [59]. Consequently, the AgNPs serve as electron mediators within the ternary heterojunction, thereby explaining changes in electron band structures. This energy-level architecture allows the ABMOT system to utilize a broader range of the spectrum, extending into the visible spectrum compared to bare TiO_2.

To further validate the charge-separation efficiency and the recombination rate of photogenerated electron-hole pairs, PL spectroscopy was also conducted, as shown in Fig. 6. The highest emission intensity was observed in pristine TiO_2, indicating a high rate of spontaneous electron-hole recombination, which limits its photocatalytic potential. Consequently, a progressive quenching of the PL emission signal is a hallmark of Type-II heterojunction formation, where the staggered band alignment between TiO_2 and Bi_2MoO_6 creates a thermodynamic driving force for electrons and holes to migrate in opposite directions [60]. Following this, the addition of Ag to the overall ternary ABMOT system exhibits the lowest PL intensity, indicating a dramatic reduction in recombination compared to both unary and binary counterparts.

This substantial quenching in the ABMOT system provides physical evidence of the sufficient transition in the electronic states of the NCs as previously observed from the UV-DRS and Kubelka-Munk plot analyses. While the UV-DRS data confirms bandgap narrowing and the SPR effect of AgNPs, the PL results confirm that these captured photons are effectively translated into long-lived charge carriers. This further confirms the role of AgNPs in forming a Schottky barrier and functioning as a directional sink that traps electrons migrating from the CBs of TiO_2 and Bi_2MoO_6 [60]. By physically separating electrons on the Ag surface from holes in the semiconductor valence band (VB), the ternary architecture suppresses radiative recombination pathways. This synergistic relationship ensures that the improved visible-light absorption, quantified by bandgap values, directly contributes to a higher density of available reactive species during photocatalysis.

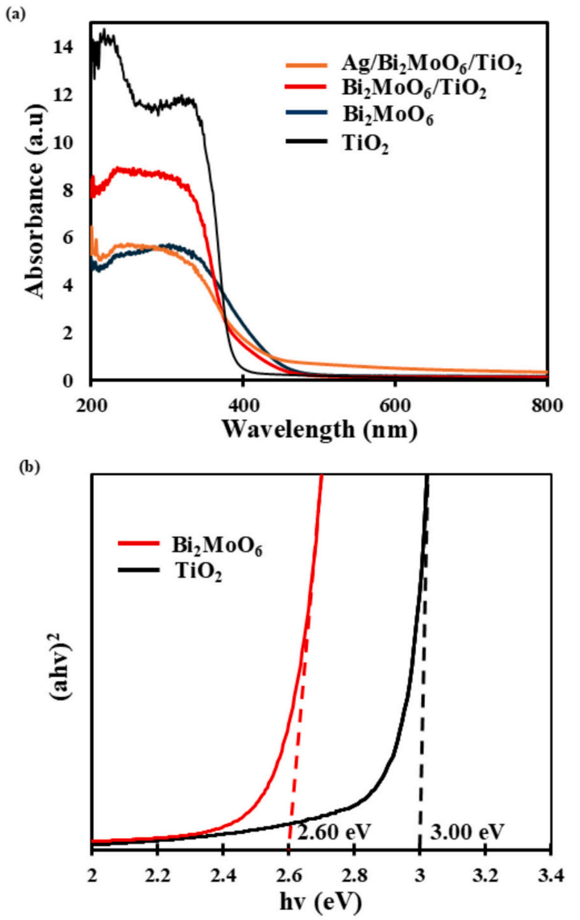

Fig. 5. (a) UV-DRS spectra and (b) Tauc's plot of TiO_2 and Bi_2MoO_6.

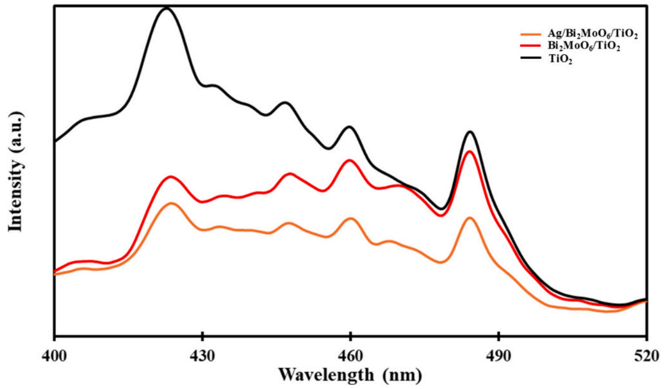

Fig. 6. PL of TiO_2, Bi_2MoO_6/TiO_2 and ABMOT ternary NC.

3.2. Photocatalytic evaluation of $Ag/Bi_2MoO_6/TiO_2$

3.2.1. Effect of dosage

Further investigation was carried out to determine the optimum dosage of ABMOT in degrading OTC under visible light for over 120 min (Fig. 7). Varying catalyst loadings of 0.3 g/L, 0.6 g/L, and 1.2 g/L were tested to evaluate the effect of catalyst dosages on the degradation process (Fig. 7a). An increase in catalyst dosage from 0.3 g/L to 0.6 g/L enhanced the photocatalytic degradation of OTC from 88.3% to 97.2% for ABMOT. However, when the dosage was increased to 1.2 g/L, a slight reduction in OTC degradation was observed for ABMOT, to 91.8%. This indicates that exceeding the optimal catalyst loading could saturate the photocatalyst surface, thereby lowering the overall removal efficiency. Although increasing the photocatalyst dosage up to a certain level can increase the number of reactive sites for photocatalysis, excessive loading could diminish the total surface area available for pollutant adsorption [61]. Increasing the catalyst dosage beyond its optimal level can also increase opacity and light scattering, which, in turn, reduces the number of photons that can penetrate the catalyst surface, a crucial factor in initiating photocatalytic reactions [62]. Notably, ABMOT also exhibited strong adsorption during the dark phase, likely due to abundant hydroxyl groups and the layered structure of Bi_2MoO_6 as observed in FTIR and SEM analysis. This results in an abundance of surface-active sites and facilitates stronger interactions with OTC molecules prior to visible-light irradiation [63]. The stronger initial adsorption of ABMOT increases pollutant concentration near active sites, thereby enabling higher degradation of adsorbed OTC on the surface of the ABMOT NCs. Therefore, the optimal dosages for both ternary photocatalysts were determined to be 0.6 g/L and were chosen for further study.

3.2.2. Effect of OTC concentration

The effect of initial OTC concentration (10–20 mg/L) at a fixed dosage of 0.6 g/L was evaluated for both ternary NCs (Fig. 7b). Minimal changes were observed as the concentration increased from 10 to 15 mg/L for ABMOT, with the degradation rate decreasing slightly from 97.2% to 93.5%. Even at 20 mg/L, ABMOT maintained a relatively high degradation efficiency of 85.9%. The reduced photodegradation rate with increasing OTC concentration could be due to excessive OTC loading on the photocatalyst surface, coupled with the accumulation of intermediates that hinder active sites and thereby suppress ROS formation. A similar finding was also observed in a previous study involving the degradation of tetracycline hydrochloride by using Bi_2MoO_6/TiO_2-based photocatalyst, whereby the degradation efficiency declined from ~87.5% to 20.0% with the increasing initial concentration from 10 mg/L to 30 mg/L [64]. Furthermore, the dark adsorption phase also revealed a notable trend for ABMOT at varying OTC concentrations. A decrease in degradation rate was observed, particularly when the concentration was increased to 20 mg/L, further proving that the layered structure of Bi_2MoO_6 and its higher hydroxyl density enable strong adsorption, allowing better removal of OTC even at high concentrations. Hence, the optimal initial concentration for OTC degradation was set to 10 mg/L (Fig. S3).

3.2.3. Photocatalytic kinetic analysis

The photocatalytic degradation kinetics of OTC over the prepared photocatalyst were evaluated using the pseudo-first order kinetic model, which is expressed as:

$$ln\left(\frac{C_o}{C_t}\right) = kt \tag{6}$$

where C_o and C_t represent the initial and time-dependent concentrations, while k is the apparent rate constant and t is the time. A linear plot of $ln\left(\frac{C_o}{C_t}\right)$ against t was plotted for TiO_2, binary Bi_2MoO_6/TiO_2, and ternary ABMOT (Fig. S4). Overall, the degradation process follows pseudo-first-order kinetics. This behaviour is consistent with typical heterogeneous photocatalytic systems under low pollutant concentrations, where the Langmuir-Hinshelwood model simplifies a pseudo-first-order expression. Similar heterojunction systems have reported similar trends in the fitting of the kinetic model [51,65].

The calculated apparent rate constants, k, were $2.7 \times 10^{-2}, 5.7 \times 10^{-3}, 5.0 \times 10^{-4}$ for ABMOT, Bi_2MoO_6/TiO_2, and TiO_2, respectively. Among them, ABMOT exhibited the highest reaction rate, which is 2.2 times higher than that of binary Bi_2MoO_6/TiO_2 and 25 times higher than TiO_2 alone, clearly demonstrating the synergistic effects of introducing Ag. Additionally, the correlation coefficients (R^2) for ABMOT, Bi_2MoO_6/TiO_2, and TiO_2 were 0.9677, 0.9354, and 0.898, respectively, which

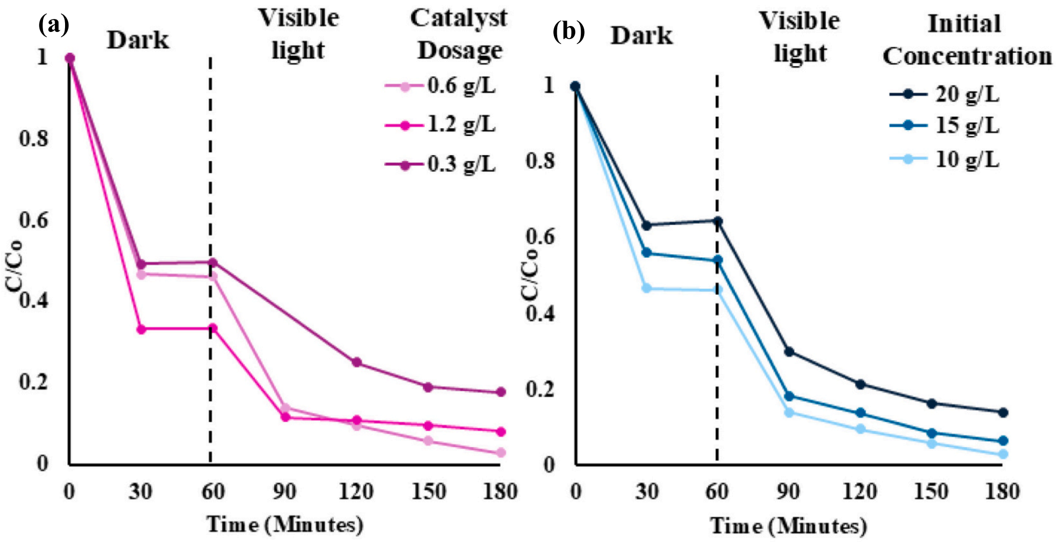

Fig. 7. Effect of (a) catalyst dosage and (b) initial pollutant concentration on the photocatalytic degradation of OTC.

confirm that the pseudo-first-order model adequately describes the reaction kinetics, with ABMOT showing the best linearity. This indicates a more consistent and controlled degradation process compared with its binary and unary counterparts. The performance of the POME-derived ABMOT is comparable to that of similar perovskite/metal oxide-based systems, confirming the overall effectiveness of the material fabrication in producing a ternary NC with an enhanced photocatalytic reaction rate and ability [65,66].

3.2.4. *Recyclability and stability study*

A recyclability study was conducted to assess the efficiency of the ABMOT ternary NC in degrading OTC over 4 consecutive cycles (Fig. 8). Photocatalyst stability is of utmost importance, as it determines scalability for larger industrial applications that require cost-effective processes. The recyclability study was performed under optimized conditions, using an ABMOT dosage of 0.6 g/L to treat 10 mg/L OTC for 120 min under visible-light irradiation. After 4 consecutive cycles, the degradation efficiency of ABMOT decreased only slightly, from 97.2% to 93.5%.

The high stability of ABMOT across consecutive cycles is primarily attributed to its ternary heterojunction structure (as evidenced by HRTEM analysis), which promotes efficient charge separation and suppresses electron-hole recombination. Similar behaviour has been observed in heterogeneous metal oxide/perovskite systems of TiO_2/$CeFeO_3$, where enhanced interfacial charge transfer contributes to sustained photocatalytic activity over repeated cycles [65]. Similarly, Bi_2MoO_6/TiO_2 systems in this study exhibit enhanced charge-transfer dynamics, as evidenced by PL characterization. Additionally, with Ag acting as an electron sink, the ternary heterojunction structure is further stabilized, thereby maintaining consistent ROS generation. This is essential for the continuous degradation of pollutants. In fact, past studies that utilized metal oxide/perovskite heterojunctions such as ZnO/$CuCo_2O_4$, TiO_2/$YMnO_3$, and $LaCeO_3$/CuO all exhibit similar trends of enhanced catalyst stability during continuous degradation cycles of malachite green (MG), with reductions of less than ~8.0% [67–69]. A summary of the recyclability performance of ABMOT, compared with NCs from past studies, is presented in Table 3. Overall, these results confirm that the ABMOT ternary NC possesses excellent reusability, structural stability, and resistance to deactivation, highlighting its strong potential for practical wastewater treatment applications.

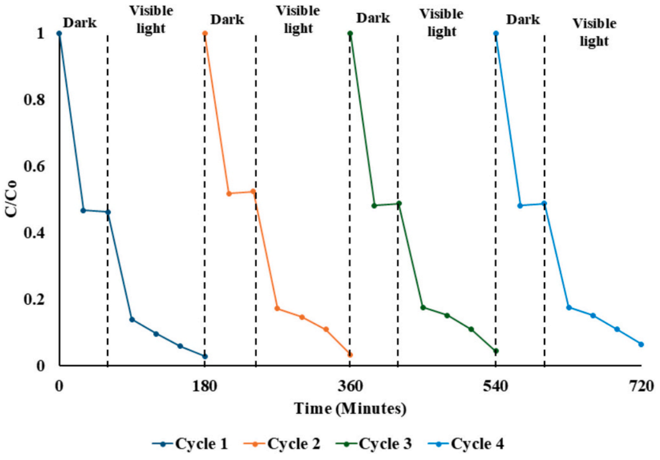

Fig. 8. Photocatalytic degradation of OTC by ABMOT after four cycles.

Nevertheless, to provide better insight into the overall stability of the ABMOT NC, the environmental stability of ABMOT was further evaluated in river and lake water matrices spiked with OTC to simulate realistic treatment conditions (Figs. 9a and 9b). A slight reduction in degradation efficiency was observed compared with distilled water, with the order: distilled water (93.57%) > river water (90.67%) > lake water (84.81%). The marginal decline in degradation rates is mainly due to the presence of dissolved ions, natural organic matter, and suspended matter in natural waters, which may compete for active sites or act as scavengers for ROS [70]. Nevertheless, retention of degradation rates above 80% across all samples further demonstrates that the ternary heterojunction maintains strong structural integrity and photocatalytic functionality even under complex environmental conditions.

Furthermore, COD analysis confirmed the mineralization capabilities and stability of ABMOT (Fig. 9c). Significant reductions in COD were achieved across all matrices, decreasing from 499.2 to 96.0 mg/L for distilled water, 576.0 to 192.0 mg/L for river water, and 729.6 to 268.8 mg/L for lake water, respectively. This reveals the oxidative degradation of OTC and its intermediates. Despite COD removal being slightly lower in lake water in comparison to the other water matrices, the overall mineralization performance remained high across the different matrices. This indicates sustained generation of oxygen species and resistance to catalyst deactivation in real water systems [71].

Potential Ag leaching was also assessed by antibacterial testing of the recycled NCs over 4 consecutive cycles against both *S. aureus* and *E. coli*

Table 3
Comparison of NCs recyclability potential.

Catalyst	Synthesis method	Pollutant	Cycles	First cycle removal (%)	Final cycle removal (%)	Ref.
$Ag/Bi_2MoO_6/TiO_2$	Green microwave-assisted synthesis	OTC	4	97.2	93.5	This study
$TiO_2/CeFeO_3$	Green sol-gel synthesis	MG	4	95.3	89.5	[65]
$YMnO_3/TiO_2$	Green synthesis	MG	5	95.3	86.6	[67]
$ZnO/CuCo_2O_4$	Green sol-gel synthesis	MG	5	93.0	81.0	[68]
$LaCeO_3/CuO$	Green synthesis	MG	3	92.8	88.8	[69]

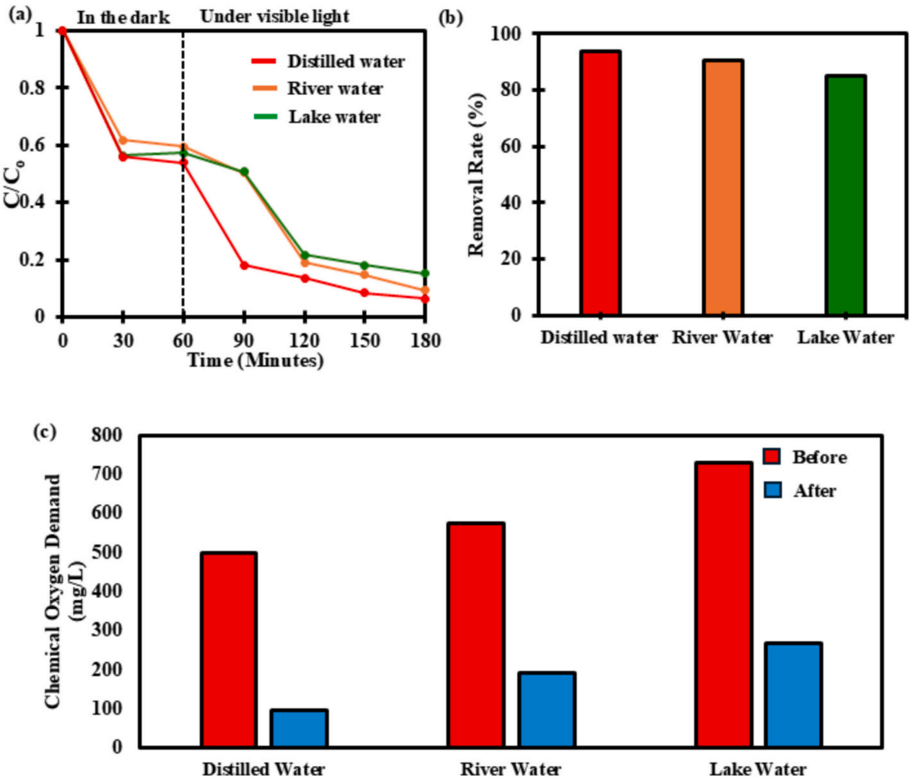

Fig. 9. (a-b) Removal of OTC in different water matrices, and (c) COD mineralization rate of OTC in different water matrices.

(Fig. 10). The inhibition zones remained relatively consistent across all cycles, with no systematic decline in antibacterial activity. This observation suggests that Ag species remained firmly anchored within the ABMOT matrix, with negligible dissolution during repeated photocatalytic operations [72]. Collectively, these findings confirm that ABMOT exhibits robust environmental durability with sustained catalytic performance, hence supporting its suitability for practical wastewater treatment.

3.3. *Scavenger study and mechanistic insight*

The superior photocatalytic performance of ABMOT ternary NCs is fundamentally rooted in their optimized electronic band structure and efficient charge separation, as confirmed by UV-DRS and PL characterization. To determine the CB and VB of the semiconductor materials, these equations were employed to calculate their respective potentials [57]:

$$E_{VB} = \chi - E^{e} + 0.5E_{g} \tag{7}$$

$$E_{CB} = E_{VB} - E_{g} \tag{8}$$

where E_{VB} and E_{CB} are the edge potentials for the valence and conduction bands, E^{e} corresponds to the energy of a free electron, which is specified as 4.5 eV, E_g are the bandgap energies of the materials, and χ is the Mulliken electronegativity of the semiconductor materials, which is $+5.81$ eV and $+ 5.08$ eV for TiO_2 and Bi_2MoO_6, respectively.

Hence, the CB and VB positions for TiO_2 were determined to be -0.19 eV and $+ 2.81$ eV, respectively, while Bi_2MoO_6 exhibited a more negative CB at -0.72 eV and a more positive VB at $+1.88$ eV [73,74]. Upon visible light irradiation, it would be assumed that the photogenerated electrons are excited to the CB of both semiconductors, and the potential gradient drives electrons from the CB of Bi_2MoO_6 to that of TiO_2, which typically describes a Type-II heterojunction. However, the interfacial charge-transfer mechanism in ABMOT is better described as a direct *Z*-scheme heterojunction rather than the conventional Type-II system, as previously deduced from optoelectronic characterization. This is further supported by the strong superoxide-scavenging activity observed in the scavenger study [75].

The incorporation of AgNPs further reinforces this Z-scheme architecture, as Ag forms Schottky junctions with TiO_2 and Bi_2MoO_6, serving as an electron mediator that facilitates rapid interfacial recombination between TiO_2 electrons and Bi_2MoO_6 holes while simultaneously trapping high-energy electrons [53]. Additionally, the SPR effect of Ag enhances visible light absorption and promotes carrier excitation. Radical scavenging experiments (Fig. S5) corroborate this mechanism as the addition of p-benzoquinone (p-bzq) significantly suppresses degradation efficiency, confirming that superoxide radicals ($\bullet O_2^{-}$) are the dominant reactive species, whereas methanol (MeOH) indicates a secondary contribution from hydroxyl radicals ($HO\bullet$). Collectively, the direct *Z*-scheme heterojunction, coupled with Ag-mediated electron transfer,

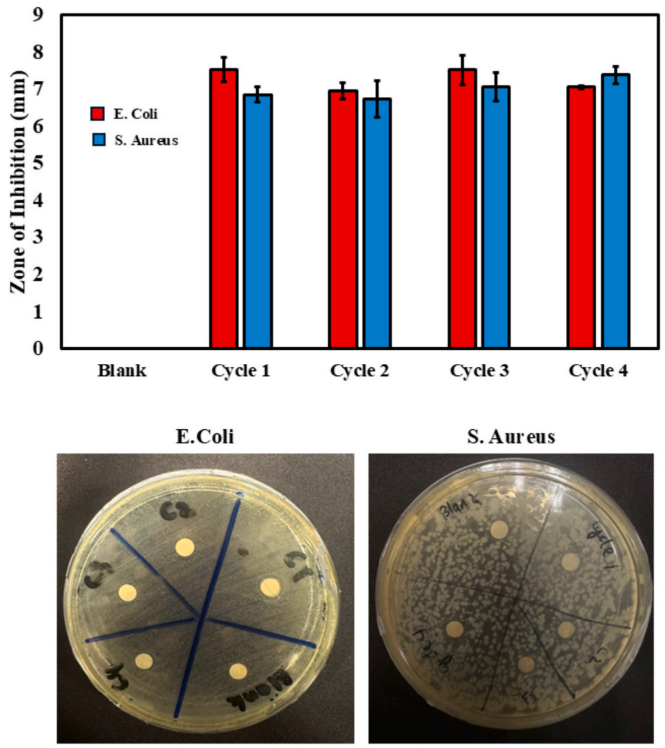

Fig. 10. Antibacterial stability and reusability of ABMOT NC against *S. aureus* and *E. coli* over four consecutive cycles.

accounts for the superior photocatalytic activity and strong redox capabilities of ABMOT NCs (Fig. 11).

This observation is consistent with ROS-based mechanistic studies in which p-benzoquinone, isopropanol, and ethylenediaminetetraacetic acid were employed as $\bullet O_2^{-}$, $HO\bullet$, and h^+ scavengers, respectively. In similar perovskite/metal oxide heterojunction systems, the suppression of photocatalytic activity upon the addition of p-bzq indicates that $\bullet O_2^{-}$ radical is the dominant reactive species [66,69]. Notably, green-synthesized $LeCeO_3$/CuO has demonstrated that coupling a wide-bandgap perovskite with a narrow-bandgap metal oxide enhances ROS generation by improving charge separation and forming an S-scheme heterojunction [69]. Similarly, $CuBi_2O_3$/CuO heterostructures exhibit enhanced visible-light absorption and promoted $\bullet O_2^{-}$ generation due to synergistic interactions between p-type semiconductors, thereby facilitating efficient pollutant degradation [66]. These findings closely parallel the behaviour observed in the ABMOT system, where the integration of Ag, Bi_2MoO_6, and TiO_2 constructs an effective Z-scheme heterojunction. This configuration enables the retention of highly reductive electrons and strongly oxidative holes, thereby maximizing the generation of $\bullet O_2^{-}$ and $HO\bullet$ radicals that drive the photocatalytic degradation of OTC. Collectively, this highlights the critical role of rational heterojunction design in optimizing charge-carrier dynamics and ROS production, ultimately enhancing photocatalytic performance. A summary of the photocatalytic mechanism can be seen in (Eqs. 10-15):

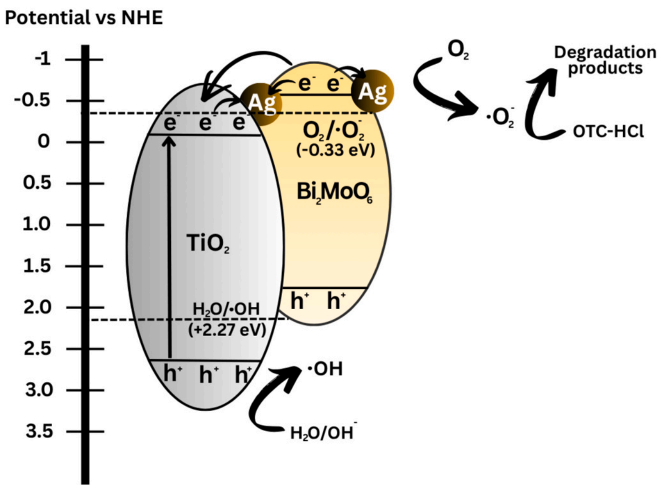

Fig. 11. Schematic illustration of the photocatalytic mechanism of ABMOT ternary NC.

$$TiO_2 + h\nu_{vis} \rightarrow e^{-}_{cb(TiO_2)} + h^{+}_{vb(TiO_2)} \tag{9}$$

$$Bi_2MoO_6 + h\nu_{vis} \rightarrow e^{-}_{cb(Bi_2MoO_6)} + h^{+}_{vb(Bi_2MoO_6))} \tag{10}$$

$$e^{-}_{cb(TiO_2)} + h^{+}_{vb(Bi_2MoO_6))} \rightarrow heat \tag{11}$$

$$e^{-}_{cb(Bi_2MoO_6)} \rightarrow Ag \tag{12}$$

$$e^{-}_{cb(Bi_2MoO_6)} + O_2 \rightarrow \bullet O_2^{-} \tag{13}$$

$$h^{+}_{vb(TiO_2)} + H_2O \rightarrow HO\bullet + h^{+} \tag{14}$$

$$\bullet O_2^{-} \text{ or } HO\bullet + OTC \rightarrow intermediates \rightarrow CO_2 + H_2O + mineralized\ products \tag{15}$$

3.4. Antibacterial properties of $Ag/Bi_2MoO_6/TiO_2$

The antibacterial activity of ABMOT was evaluated against the Gram-negative *E. coli* and the Gram-positive *S. aureus* using the disk diffusion method. Antibacterial activity was evaluated by measuring the zone of inhibition (ZOI) induced by the photocatalyst (Fig. 12). ABMOT was compared with its unary and binary counterparts at a fixed concentration to assess antibacterial activity. For unary and binary samples of TiO_2, Bi_2MoO_6, and Bi_2MoO_6/TiO_2, no measurable ZOIs were observed, suggesting negligible antibacterial properties. These results corroborate previous studies on NCs containing TiO_2 and Bi_2MoO_6, without other metal-based dopants or oxides in the ternary photocatalyst matrix [76,77]. The main reason for this observation is the non-toxicity of Ti-, Bi-, and Mo-based oxides. In most cases, the antibacterial activity of Ti-, Bi-, and Mo-based metal oxides arises from the generation of reactive species that damage cells. However, in the disc diffusion method, the absence of light significantly dampens the antibacterial activity.

The presence of Ag in ABMOT produced clear ZOIs, confirming antibacterial activity induced by the AgNPs within the composite matrix. Ag is known to exhibit antibacterial properties due to the dissolution of Ag^+ ions, which readily attack microbial cell membranes [78]. Increasing the Ag dosage from 1% to 10% enhanced the ZOI, with ABMOT showing an increase from 6.23 ± 1.05 mm to 13.68 ± 0.36 mm against *E. coli* (Fig. 12a). In the case of *S. aureus*, increasing Ag content in ABMOT yielded similar results with an increase in ZOIs from 7.35 ± 0.66 mm to 10.31 ± 1.07 mm (Fig. 12b). These results suggest that the antibacterial activity is predominantly driven by AgNPs, which likely enhance oxidative stress and disrupt bacterial cell membranes, thereby disrupting essential cellular functions and leading to cell death [79,80]. Additionally, the antibacterial mechanisms of the two ternary composites differ, as reflected in their distinct ZOIs.

Moreover, a study on the effect of catalyst dosage on antibacterial activity was conducted to determine the optimal dosage for bacterial inhibition (Fig. 13). Increasing catalyst dosage led to larger ZOIs. However, the ZOI against gram-negative *E. coli* began to decline once the dosage exceeded 6 g/L, although the ZOI increased to 10 g/L (Fig. 13a). This could be attributed to saturation of interactions between the nanomaterials and bacterial cells. On the contrary, when similar conditions were conducted with gram-positive *S. aureus*, a proportional

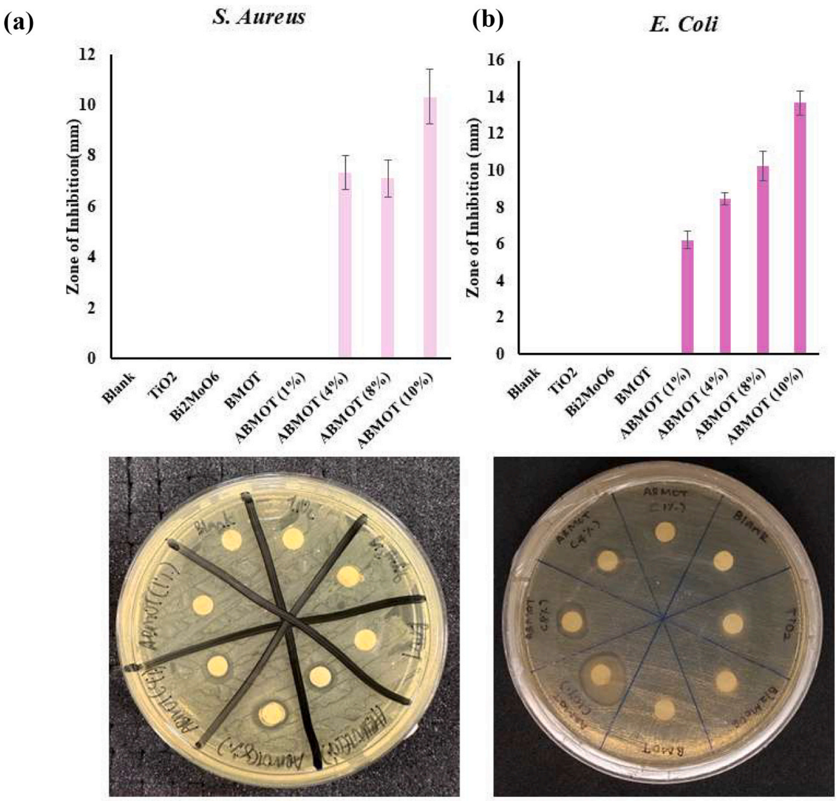

Fig. 12. Antibacterial activity of ABMOT (a) gram-negative *E. coli* and (b) gram-positive *S. aureus* bacteria.

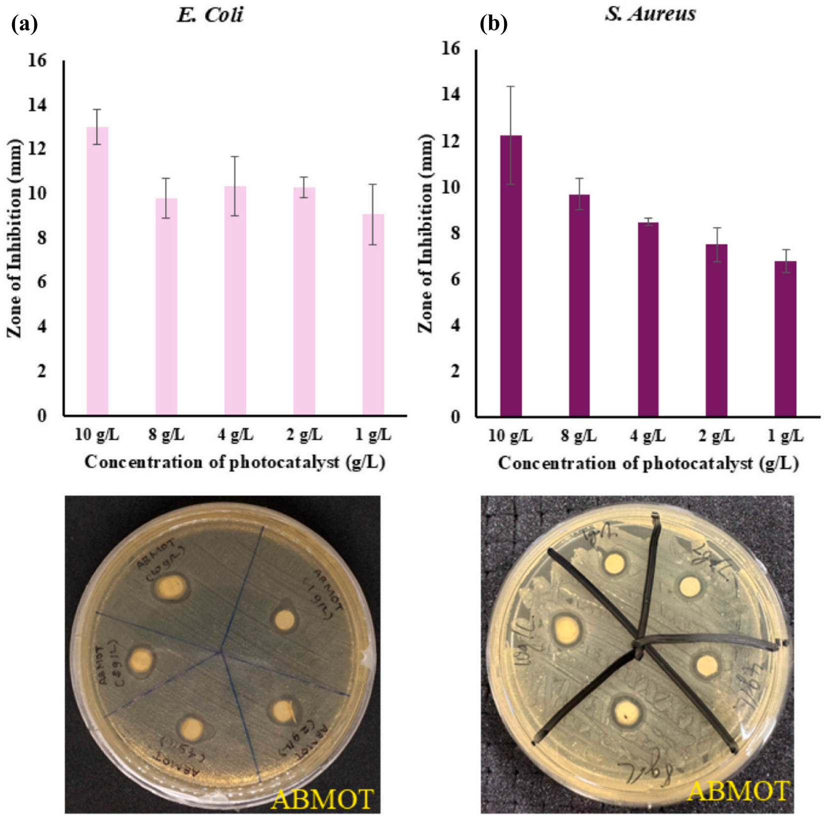

Fig. 13. Effect of catalyst dosage on antibacterial activity by ABMOT against (a) *E. coli* and (b) *S. aureus* bacteria.

relationship between concentration and ZOIs was observed (Fig. 13b). This is because a higher concentration of nanomaterials is needed for a more effective disruption of bacterial activities, as gram-negative bacteria possess a thicker peptidoglycan layer compared to gram-positive bacteria [81]. From a collective perspective, the overall photocatalytic performance and antibacterial activity of ABMOT are promising for applications in water treatment and disinfection.

3.5. Application with PAN membrane

3.5.1. Characterization of Ag/Bi_2MoO_6/TiO_2@PAN

To investigate the physicochemical changes upon NC incorporation, FTIR analysis was employed to evaluate the chemical interactions and the retention of functional groups of the NCs within the membrane matrix. Comparison between bare PAN membranes and ABMOT@PAN was carried out within the range of 400–4000 cm^{-1}, as observed in Fig. 14a. All samples displayed characteristic PAN absorption bands, including the strong nitrile (–C ≡ N) stretching at ~2242 cm^{-1}, and bending vibrations of C—H at ~1450 cm^{-1}. Upon integration of ABMOT, slight shifts and changes in transmittance intensity were observed in the regions around 1630 cm^{-1} and 1000–700 cm^{-1}. These alterations suggest interactions between the PAN polymer chains and surface functionalities of the NCs [82]. For instance, the broadband around 3400 cm^{-1}, associated with O—H bending, showed enhanced intensity in the ABMOT@PAN samples, possibly due to increased surface hydroxylation from the incorporated metal oxides. In the

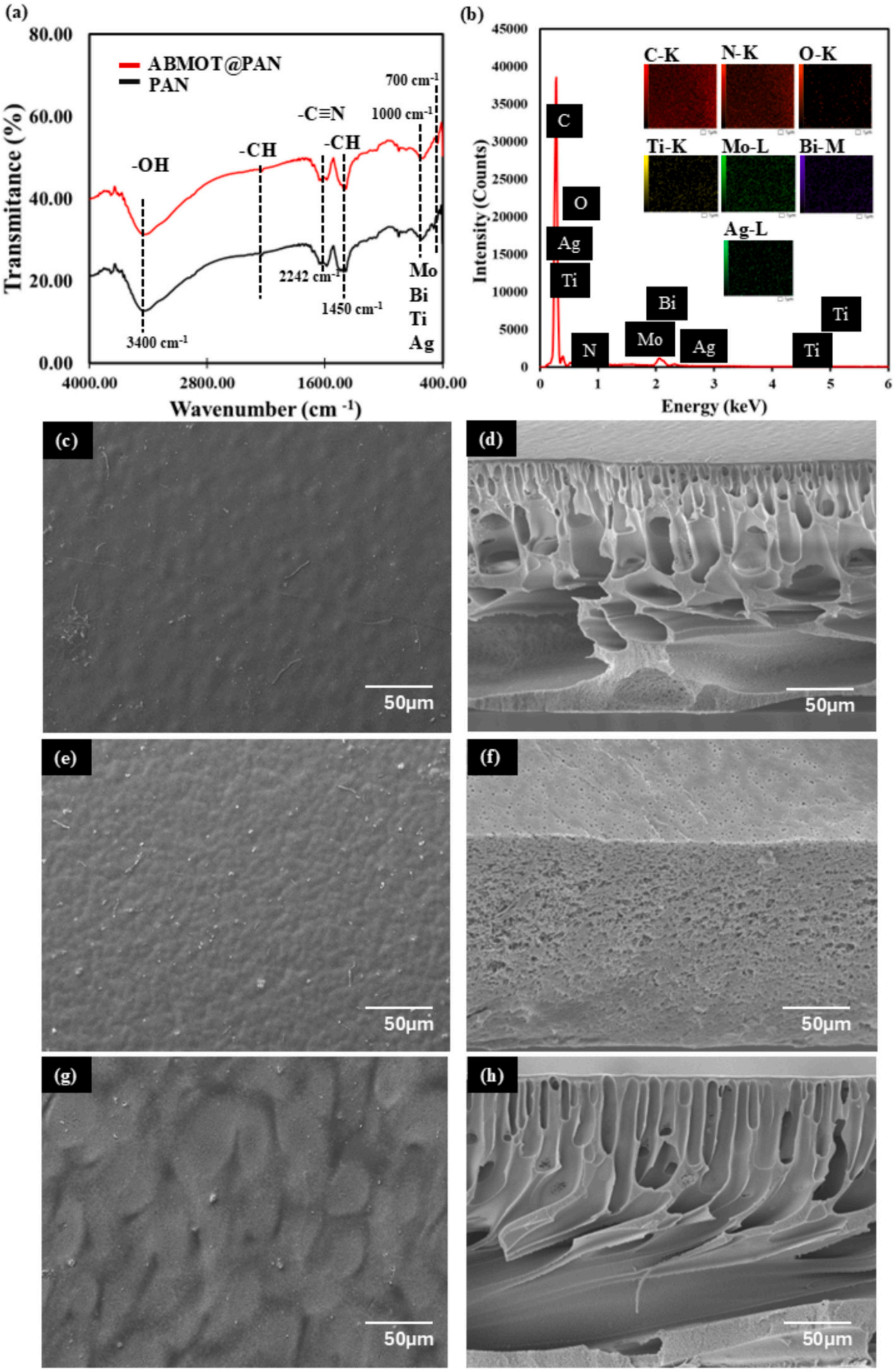

Fig. 14. (a) FTIR spectra of pristine PAN and ABMOT@PAN membranes, (b) EDX spectra and elemental mapping of ABMOT@PAN membrane, and SEM micrograph for membrane surface and cross section of (c-d) PAN, (e-f) ABMOT@PAN (1%), and (g-h) ABMOT@PAN (2%).

fingerprint region (~700–1000 cm^{-1}), additional features may correspond to stretching vibrations of metal–oxygen (M–O) bonds from Bi—O, Mo—O, Ti—O, or Ag—O linkages, further supporting successful NC integration. This result confirms chemical interactions between NC and PAN within the NC-membrane matrices, thereby validating the incorporation of ABMOT into PAN membranes.

Additionally, ternary NC incorporation into the PAN membrane was validated using SEM-EDX analysis (Figs. 14b-d). The bare PAN membrane exhibited a relatively smooth and featureless surface, characteristic of pristine PAN prepared via phase inversion, with no visible particulate deposits or irregular surface structures (Fig. 14c). This smoothness indicates a uniform polymer film formation in the absence of NC additives [83]. The 1 wt% ABMOT@PAN membrane resulted in a noticeably more textured surface with fine granules distributed across it, suggesting that the NC particles were successfully embedded within and partially exposed on the membrane surface (Fig.14d). Increasing the NC loading to 2 wt% further intensified the observed surface texturing. The 2 wt% ABMOT@PAN membrane surfaces appeared even more irregular, with a combination of textured wave-like features and larger exposed particle clusters (Fig. 14e).

Moreover, a distinct morphological evolution in each membrane cross-section was also observed as the ABMOT concentration increased in the mixed-NC membrane matrix. While pristine PAN membranes displayed a compact structure (Fig. 14d), the introduction of 1% wt ABMOT into the membrane matrix resulted in a transition towards a more sponge-like porous network as observed in Fig. 14f). This was likely caused by the slight increase in the casting solution viscosity at low NC loading, which hinders the rapid penetration of water leading to a delayed demixing process by hindering the rapid exchange between the DMSO solvent and the water coagulant [84].

Interestingly, at 2% wt loading (Fig. 14h), the cross-section reveals the emergence of a more finger-like microporous structure extending from the top surface into a sponge-like sublayer. This transition suggests that at higher NC concentration, the inherent hydrophilicity Ag, Bi_2MoO_6, and TiO_2 from the ternary NC systems begins to override the viscosity effect of NC loading. The presence of metal oxide functionalities, especially TiO_2 and Bi_2MoO_6, as indicated by the OH- stretching in FTIR spectra at ~3400 cm^{-1}, promoted the rapid influx of water coagulant during the phase inversion process. This accelerated instantaneous demixing facilitates the formation of elongated macrovoids. The presence of a sponge-like sublayer is often associated with superior mechanical properties compared to finger-like structures, which is crucial, as it also enhances overall membrane lifespan [85]. Furthermore, EDX elemental mapping verified the presence of each element in both ABMOT@PAN NC membranes (Fig. 14b).A summary of the elemental composition is tabulated in Table 4. The absence of some elements, Ag and Bi, within ABMOT@PAN membranes is attributed to the low amount of NCs compared to the mass of PAN in the NC-membrane matrix [86]. Nevertheless, trace amounts are still detected in the system, validating the sequence of NC incorporation.

Table 4
Elemental composition of ABMOT@PAN membrane.

Elements	Mass (%)
Ti	0.24 ± 0.04
O	2.92 ± 0.05
Ag	Not detected
Bi	Not detected
Mo	2.45 ± 0.06
C	72.45 ± 0.07
N	21.94 ± 0.17

Table 5
Porosity and water contact angle of PAN, 1% ABMOT@PAN, and 2% ABMOT@PAN.

Membrane	Membrane Characteristic	
	Porosity (%)	Water Contact Angle (°)
PAN	87.42 ± 5.76	57.15 ± 2.00
1% ABMOT@PAN	89.36 ± 1.40	45.49 ± 3.02
2% ABMOT@PAN	90.54 ± 0.47	48.49 ± 0.33

Further evaluation of the membrane porosity was also done via the gravimetric method to determine the influence of incorporating ABMOT ternary NCs on the internal void volume of the PAN membrane matrix. As summarized in Table 5, the overall porosity of the membranes increased from 77.76% for the pristine PAN membrane to 89.36% and 90.54% for the 1% wt and 2% wt ABMOT@PAN membranes, respectively. This progressive increase in porosity can be linked to the morphological transition observed in the SEM cross-section, which is mainly driven by the instantaneous demixing mechanism during phase inversion as previously discussed. The hydrophilic nature of the ternary NC components accelerates the exchange between DMSO solvent and the water coagulant [87]. This causes expansion of the polymer network and formation of the elongated, finger-like macrovoids observed in the SEM, as previously discussed.

The shift in membrane porosity is a critical structural precursor to the membrane's permeation capabilities. While hydraulic permeability is highly sensitive to porosity, according to the Hagen-Poiseuille relationship, a highly porous structure with up to 90.54% porosity exhibits a non-linear reduction in hydraulic resistance by creating high-flux pathways for effluent [88]. Additionally, while the difference in porosity between 1% wt NC and 2% wt NC may appear subtle, it still indicates a more interconnected pore network that minimizes dead-end channels. The hierarchical architecture, which combines a porous, finger-like top layer with a spongy sublayer for mechanical support, ensures maximum permeability without sacrificing structural integrity [88].

Finally, the surface wettability of the membranes, a critical factor influencing permeation flux, was quantitatively assessed using water contact angle (WCA) measurements. As shown in Fig. 15, the pristine PAN membrane exhibited a WCA of 57.17°. When 1% wt ABMOT NC was loaded, the WCA showed a decrease to 45.48°, which indicates a substantial enhancement in the surface hydrophilicity. Interestingly, at a higher loading of 2% wt ABMOT NC, the WCA slightly increased to 48.49°. Regardless, it was still considerably lower than that of the pristine PAN membranes. The initial sharp decline in WCA at 1% wt loading is consistent with the transition to a sponge-like porous network, which increases the effective surface area for water interaction. Following this, the slight increase in contact angle observed with 2% wt loading can be attributed to changes in surface topography. As NC loading increases, larger particle clusters and wave-like features can trap

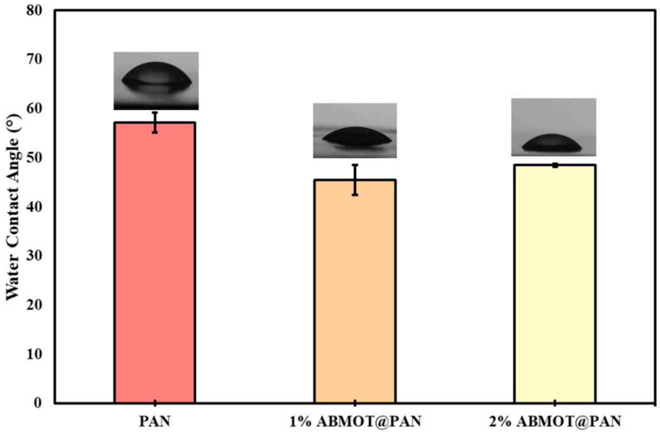

Fig. 15. Water contact angle of pristine PAN, 1% ABMOT-loaded PAN, and 2% ABMOT-loaded PAN membranes.

microscopic pockets of air. This phenomenon is often described by the Cassie-Baxter model, which can slightly offset the hydrophilic gains provided by the chemistry of NC [89]. Nevertheless, both NC loading percentages show a reduction in WCA, indicating that enhanced hydrophilicity works in tandem with high porosity to facilitate rapid water infiltration through the finger-like macrovoids, ensuring high permeability. A summary of the WCA is also provided in Table 4.

3.5.2. *Permeation test of ABMOT@PAN*

Pure water flux (PWF) analysis was conducted to evaluate the permeability of bare PAN and ABMOT-integrated PAN membranes (Fig. 16a). The bare PAN membrane exhibited the lowest flux value of 129.17 $L{\cdot}m^{-2}{\cdot}h^{-1}$**,** which is consistent with its relatively smooth texture and lower porosity as shown in the characterization of the membranes. Incorporating ABMOT into the PAN matrix led to a consistent enhancement in PWF. At a loading of 1 wt%**,** the ABMOT@PAN membrane achieved a flux of 144.39 $L{\cdot}m^{-2}{\cdot}h^{-1}$ and even reached 163.48 $L{\cdot}m^{-2}{\cdot}h^{-1}$ at 2 wt% loading. The observed enhancement of the PWF is directly supported by the structural evolution as depicted in the cross-section SEM and the gravimetric analysis of the membranes. The transition from a compact structure to a more porous matrix with finger-like macropores significantly reduced the hydraulic resistance. Furthermore, a reduced water contact angle enables faster wetting and infiltration, thereby providing a more efficient pathway for water transport within the membrane matrix [90].

The rejection rate testing (Fig. 16b) showed that the bare PAN membrane had the lowest OTC removal efficiency at 44.88%. whereas the integration of 1% wt and 2% wt ABMOT NCs significantly bolstered the rejection factor up to 72.30% and 85.69%, respectively. With respect to each membrane's characteristics, the OTC rejection mechanism in these NC incorporated membranes is mainly governed by a synergistic combination of size exclusion and surface-mediated interactions. Firstly, the morphological transition from a sponge-like porous network to a hierarchical finger-like macrovoid structure with a specialized pore channel (as seen in Fig. 14h) enhances the physical sieving effect. While the overall porosity increased, the successful embedding of ABMOT NCs within the polymer matrix, as confirmed by EDX elemental mapping, likely narrows the effective pore neck size or increases the tortuosity of the separation layer, effectively trapping OTC molecules through size exclusion. Secondly, the hydroxyl groups and metal-oxygen sites in ABMOT NCs provide active sites for electrostatic interactions and hydrogen bonding. This increases the adsorption-based retention of contaminants during filtration [91,92]. The combined effects of size-exclusion and surface-interaction mechanisms increase the efficiency of OTC rejection.

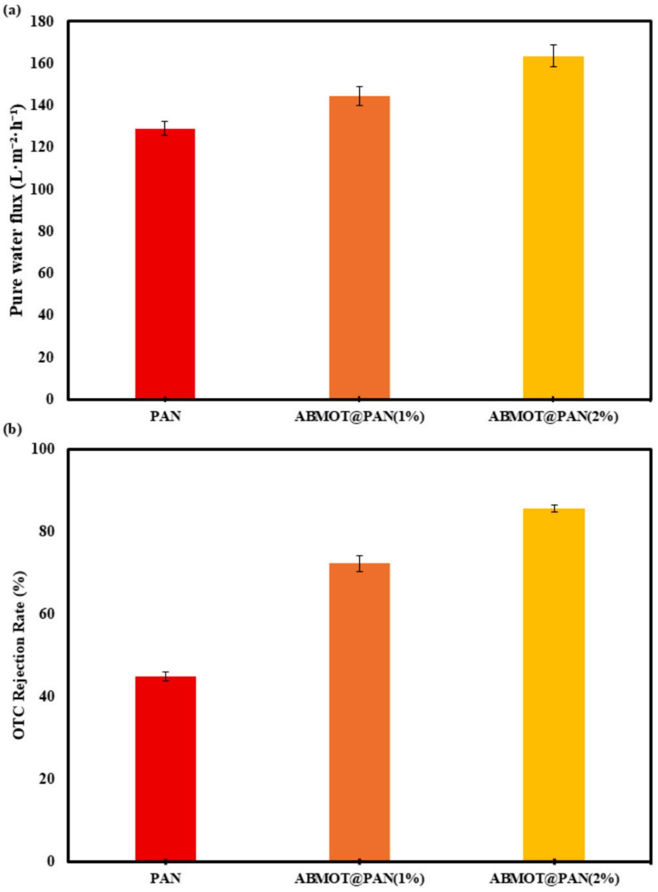

Fig. 16. (a) Pure water flux and (b) OTC rejection efficiency of pure PAN, and ABMOT@PAN membranes.

Although these evaluations were conducted strictly under non-photocatalytic filtration conditions, the significant boost in rejection efficiency proves that the incorporation of ABMOT NCs provides both structural and physicochemical modifications that enhance the membrane's affinity towards OTC. The evolution of the membrane's surface and cross-sectional morphology, wettability, and porosity all contribute to maximized retention potential. This strong rejection performance, coupled with relatively high porosity and hydrophilicity, positions the complex ternary ABMOT NCs as sufficiently compatible for incorporation into advanced PAN membrane matrices. Ultimately, the successful harmonization of robust physical rejection with the inherent photocatalytic potential of ABMOT systems underscores the viability of using sustainable, multi-component heterojunctions for next-generation advanced wastewater remediation technologies.

4. Conclusions

A ternary ABMOT NC was successfully fabricated using a combination of sol-gel, green hydrothermal synthesis, and microwave-assisted deposition methods. Comprehensive structural, morphological, and optical analyses (FTIR, XRD, SEM–EDX, TEM, XPS, PL, and UV–Vis DRS) confirmed the formation of a well-integrated and stable heterojunction system, in which TiO_2, Bi_2MoO_6, and plasmonic Ag nanoparticles are intimately coupled. This hierarchical integration enhanced visible-light absorption and efficient charge separation, arising from the synergistic interfacial interactions between Bi_2MoO_6 and TiO_2 and from the SPR effect of Ag. The photocatalytic performance evaluation revealed that ABMOT exhibited exceptional OTC degradation under visible-light irradiation, maintaining high efficiency across a wide range of pollutant concentrations. The structural robustness of the ternary heterojunction was further evidenced by its excellent stability over four consecutive cycles, with only marginal loss of activity, highlighting the material's durability. In parallel, antibacterial studies revealed that incorporating AgNPs endowed ABMOT with potent activity against *E. coli* and *S. aureus*, whereas the unary and binary counterparts exhibited negligible inhibition, demonstrating the unique contribution of Ag. Beyond powder-based applications, ABMOT was successfully immobilized within PAN membranes, extending its functionality into a hybrid photocatalytic-separation platform. The resulting ABMOT@PAN membranes showed enhanced hydrophilicity, increased water flux, and markedly improved OTC rejection relative to pristine PAN membranes. Importantly, even in the absence of light activation, incorporation of the NC altered membrane morphology and created additional adsorption and interaction sites, indicating that the advanced ABMOT material retains its intrinsic structural and interfacial properties upon integration into a solid-state membrane architecture, thereby enabling enhanced separation behaviour. Collectively, this work provides the first successful demonstration of POME-derived precursors for synthesizing a complex ternary NC and integrating it into a functional membrane system. The findings advance the design of visible-light-responsive photocatalysts and establish a circular-economy-driven pathway to transform agro-industrial waste into high-value materials. These insights are expected to inform the development of next-generation photocatalytic and membrane-based materials for advanced separation and environmental technologies.

CRediT authorship contribution statement

Devagi Kanakaraju: Writing – review & editing, Supervision, Resources, Project administration, Methodology, Funding acquisition, Conceptualization. **Danielson Ngo Joseph:** Writing – original draft, Methodology, Investigation, Formal analysis, Data curation. **Lim Ying Chin:** Writing – review & editing, Formal analysis. **Khairul Anwar bin Mohamad Said:** Writing – review & editing. **Micky Vincent:** Writing – review & editing. **Md. Rezaur Rahman:** Writing – review & editing.

Declaration of competing interest

The authors declare that they have no known competing financial interests or personal relationships that could have appeared to influence the work reported in this paper.

Acknowledgement

The authors are grateful for the financial support from Universiti Malaysia Sarawak under the VC- High Impact Research Grant (UNI/F07/VC-HIRG/85506/P10-01/2022).

Appendix A. Supplementary data

Supplementary data to this article can be found online at https://doi.org/10.1016/j.mseb.2026.119520.

Data availability

Data will be made available on request.

References

[1] A. Arumugam, K.E. Lee, P.Y. Ng, A.S. Shamsuddin, A. Zulkifli, T.L. Goh, Pharmaceuticals as emerging pollutants: implications for water resource management in Malaysia, Emerging Contaminants 11 (2025) 100470.

[2] S.N. Ahmed, W. Haider, Heterogeneous photocatalysis and its potential applications in water and wastewater treatment: a review, Nanotechnology 29 (2018) 342001.

[3] A. Anvari, M. Amoli-Diva, R. Sadighi-Bonabi, Concurrent photocatalytic degradation and filtration with bi-plasmonic TiO_2 for wastewater treatment, Micro Nano Lett. 16 (2021) 194–202.

[4] D.G. Della Rocca, R.M. Peralta, R.A. Peralta, R.D.F. Peralta Muniz Moreira, Recent development on Ag_2MoO_4-based advanced oxidation processes: a review, React. Kinet. Mech. Catal. 132 (2021) 1–35.

[5] P. Kumari, A. Kumar, Advanced oxidation process: a remediation technique for organic and non-biodegradable pollutant, Results Surf. Interfaces 11 (2023) 100122.

[6] N. Celebi, M.Y. Aydin, F. Soysal, Y.O. Ciftci, K. Salimi, Ligand-free fabrication of au/TiO_2 nanostructures for plasmonic hot-electron-driven photocatalysis: Photoelectrochemical water splitting and organic-dye degradation, J. Alloys Compd. 860 (2021) 157908.

[7] M. Dahl, Y. Liu, Y. Yin, Composite titanium dioxide nanomaterials, Chem. Rev. 114 (2014) 9853–9889.

[8] M. Arif, M. Zhang, B. Qiu, J. Yao, Q. Bu, A. Ali, T. Muhmood, I. Hussian, X. Liu, B. Zhou, X. Wang, Synergistic effect of ultrathin thickness and surface oxygen vacancies in high-efficiency Ti-mediated Bi_2MoO_6 for immense photocatalytic nitrofurantoin degradation and Cr(VI) reduction, Appl. Surf. Sci. 543 (2021) 148816.

[9] D. Wang, J.F.C. Loo, J. Chen, Y. Yam, S.-C. Chen, H. He, S.K. Kong, H.P. Ho, Recent advances in surface plasmon resonance imaging sensors, Sensors 19 (2019) 1266.

[10] L. Wu, Y. Luo, S. Zhou, Z. Wu, X. Chen, Fabrication of Ag-TiO_2 functionalized activated carbon for dyes degradation based on tea residues, Colloid Surf. A: Physiochem. Eng. Asp. 627 (2021) 127130.

[11] X. Yang, J. Liang, H. Fu, X. Ran, X. An, Fabrication of Au-Ag@TiO_2 ternary core-shell nanostructures with enhanced sunlight photocatalytic activity, Powder Technol. 404 (2022) 117463.

[12] F. Yi, Y. Liu, Y. Chen, J. Zhu, Q. He, C. Yang, D. Ma, J. Liu, Dual S-scheme g-C_3N_4/Ag_3PO_4/g-C_3N_5 photocatalysts for removal of tetracycline pollutants through enhanced molecular oxygen activation, Chin. Chem. Lett. 36 (2025) 110544.

[13] C. Yang, Z. Zhang, X. Liu, G. Zhou, J. Tang, J. Liu, Sustainable photocatalytic process using non-silver agent ZnO/P-g-C_3N_4/$Sr_2MgSi_2O_7$:Eu^{2+},Dy^{3+} for antibacterial activity, J. Alloys Compd. 1005 (2024) 176017.

[14] S.N. Sari, R.M. Surya, D.O.B. Apriandanu, C.W. Lai, Y. Yulizar, A breakthrough sustainable synthesis of Er_2O_3 nanoparticles using *Dendrocalamus asper* natural extract for effective photocatalytic response, Catal. Today 467 (2026) 115655.

[15] M. Rahayu, R.D.F. Irbati, V.R. Ananda, M.R. Yusuf, D.O.B. Apriandanu, A. Umar, Y. Yulizar, Structural and optical tuning of HfO_2 nanoparticles synthesized via sterculia oblongata: role of extraction solvents and calcination temperature, Vacuum 242 (2025) 114718.

[16] C. Ofori-Boateng, K.T. Lee, Sustainable utilization of oil palm wastes for bioactive phytochemicals for the benefit of the oil palm and nutraceutical industries, Phytochem. Rev. 12 (2013) 173–190.

[17] I. Lucas-Gómez, G. Carrasco-Torres, D. Bahena-Uribe, J. Santoyo-Salazar, E. Fernández-Martínez, I. Sánchez-Crisóstomo, J.A. Pescador-Rojas, J.E. Aparicio-Burgos, Green synthesis of silver nanoparticles with phytosterols and betalain pigments as reducing agents present in cactus *Myrtillocactus geometrizans*, MRS Adv. 5 (2020) 3361–3369.

[18] S. Shankar, J.-W. Rhim, Tocopherol-mediated synthesis of silver nanoparticles and preparation of antimicrobial PBAT/silver nanoparticles composite films, LWT Food Sci. Technol. 72 (2016) 149–156.

[19] H. Sowani, P. Mohite, S. Damale, M. Kulkarni, S. Zinjarde, Carotenoid stabilized gold and silver nanoparticles derived from the actinomycete *Gordonia amicalis* HS-11 as effective free radical scavengers, Enzym. Microb. Technol. 95 (2016) 164–173.

[20] P.P. Gan, S.H. Ng, Y. Huang, S.F.Y. Li, Green synthesis of gold nanoparticles using palm oil mill effluent (POME): a low-cost and eco-friendly viable approach, Bioresour. Technol. 113 (2012) 132–135.

[21] S.P. Pradhan, S. Swain, N. Sa, S.N. Pilla, A. Behera, P.K. Sahu, S. Chandra Si, Photocatalysis of environmental organic pollutants and antioxidant activity of flavonoid conjugated gold nanoparticles, Spectrochim. Acta A Mol. Biomol. Spectrosc. 282 (2022) 121699.

[22] A.S. Aliero, N.A. Zawawi, N.A.N.N. Malek, B.J. Usman, M.H. Asraf, J. Matmin, M. Isah, Harnessing palm oil mill effluent for the green synthesis of silver nanoparticles: optimization via response surface methodology and assessment of antibacterial activity, J. Inorg. Organomet. Polym. Mater. 35 (2024) 3580–3596.

[23] S.A. Rahmah, D.O.B. Apriandanu, H.A. Ariyanta, Y. Yulizar, Unveiling the z-scheme boosting visible-light photocatalysis in green-derived ZnO/$EuFeO_3$ nanocomposites for degradation of organic pollutant, J. Phys. Chem. Solids 210 (2026) 113325.

[24] A. Khaerunnisa, T. Ditalistya, F. Amalia, D.O.B. Apriandanu, D. Annas, I. Abdullah, Y. Yulizar, Visible-light-driven photocatalytic degradation of malachite green using green-synthesized TiO_2/$CeZrO_4$ S-scheme nanocomposites via bitter melon (*Momordica charantia* l.) leaf extract, Appl. Surf. Sci. 723 (2026) 165526.

[25] A. Elrasheedy, N. Nady, M. Bassyouni, A. El-Shazly, Metal organic framework based polymer mixed matrix membranes: review on applications in water purification, Membranes 9 (2019) 88.

[26] D. Kanakaraju, A. Chandrasekaran, Y.C. Lim, Facile synthesis and characterization of a visible light-active ternary TiO_2/ZnS/g-C_3N_4 heterostructure for multipollutant degradation, J. Mater. Sci. 59 (2024) 810–827.

[27] S. Kanwal, M.I. Khan, M. Uzair, M. Fatima, M.A. Bukhari, Z. Saman, H.I. Elsaeedy, S. Urram, Z. Mufarreh Elqahtani, N. Alwadai, A facile green approach to the synthesis of Bi_2WO_6@V_2O_5 heterostructure and their photocatalytic activity evaluation under visible light irradiation for RhB dye removal, Arab. J. Chem. 16 (2023) 104685.

[28] M. Selvamani, S. Balachandran, A.V. Kesavan, V. Vinoth, Bi_2MoO_6 nano-flowers for bi-functional application: anticancer activity against B16F10 (mice melanoma) and photocatalytic dye degradation, Surf. Interfaces 42 (2023) 103340.

[29] Y. Liu, L. Li, T. Hu, X. Zhu, H. Wang, W. Zhang, S. Chen, S. Cheng, Y. Cao, Y. Li, Enhanced photocatalytic performance of multifunctional composite Ag-Ag_2Se@CdSe/3DOM TiO_2 with dual Z-scheme heterostructures coupling Ag NPs: degradation, hydrogen production and antibacterial activity, J. Alloys Compd. 1021 (2025) 179571.

[30] APHA. Chemical Oxygen Demand (COD): Standard Methods for the Examination of Water and Wastewater, 18th Ed, American Public Health Association, American Water Works Association, Washington, D.C, 1999.

[31] A.Z. Sueraya, M.R. Rahman, K.A.B.M. Said, M. Namakka, D. Kanakaraju, J.Y. Al-Humaidi, S.M. Al-Baqami, M.M. Rahman, M.U. Khandaker, Impact of titanium dioxide/graphene in polyvinylidene fluoride nanocomposite membrane to intensify methylene blue dye removal, antifouling performance, and reusability, J. Appl. Polym. Sci. 141 (2024) e56257.

[32] R. Liu, X. Li, J. Huang, H. Pang, Q. Wan, K. Luo, Y. Pang, L. Wang, Synthesis and characterization of g-C_3N_4/Ag_3PO_4/TiO_2/PVDF membrane with remarkable self-cleaning properties for rhodamine b removal, Int. J. Environ. Res. Public Health (2022) 15551.

[33] M. Tavakolmoghadam, A. Mokhtare, F. Rekabdar, M. Esmaeili, A. Hossein Khanli Khaneghah, A predictive model for tuning additives for the fabrication of porous polymeric membranes, Mater. Res. Express 7 (2020) 015312.

[34] H. Huang, Y. Xu, Z. Lu, A. Zhang, D. Zhang, H. Xue, P. Dong, J. Zhang, T. Goto, Highly permeable and dye-rejective nanofiltration membranes of TiO_2 and Bi_2S_3 double-embedded Ti_3C_2Tx with a visible-light-induced self-cleaning ability, J. Mater. Res. Technol. 18 (2022) 4156–4168.

[35] L. Cai, Y. Zhou, Z. Wang, J. Chen, L. Ji, J. Guo, Y. Wang, W. Song, J. Liu, Preparation and evaluation of a hierarchical Bi_2MoO_6/MSB composite for visible-light-driven photocatalytic performance, RSC Adv. 9 (2019) 38280–38288.

[36] Z. Zhang, T. Zheng, J. Xu, H. Zeng, Polythiophene/Bi_2MoO_6: a novel conjugated polymer/nanocrystal hybrid composite for photocatalysis, J. Mater. Sci. 51 (2016) 3846–3853.

[37] R. Das, P. Kumar, A.K. Singh, S. Agrawal, S. Albukhaty, I. Bhattacharya, K. N. Tiwari, S.K. Mishra, A.K. Tripathi, F.A. AlMalki, A.K. Alzubaidi, W.J. Al-Kaabi, V.D. Rajput, Z.T. Al-aqbi, Green synthesis of silver nanoparticles using *Trema Orientalis* (L.) extract and evaluation of their antibacterial activity, Green Chem. Lett. Rev. 18 (2025) 2444679.

[38] W.M. Shume, H.C.A. Murthy, E.A. Zereffa, A review on synthesis and characterization of Ag_2O nanoparticles for photocatalytic applications, J. Chem. 2020 (2020) 5039479.

[39] R. Katal, S. Masudy-Panah, M. Tanhaei, M.H.D.A. Farahani, H. Jiangyong, A review on the synthesis of the various types of anatase TiO_2 facets and their applications for photocatalysis, Chem. Eng. J. 384 (2020) 123384.

[40] L. Ye, J. Mao, J. Liu, Z. Jiang, T. Peng, L. Zan, Synthesis of anatase TiO_2 nanocrystals with {101}, {001} or {010} single facets of 90% level exposure and liquid-phase photocatalytic reduction and oxidation activity orders, J. Mater. Chem. A. 1 (2013) 10532–10537.

[41] H.S. Tan Sian Hui Abdullah, S.N. Aqlili Riana Mohd Asseri, W.N. Khursyiah Wan Mohamad, S.-Y. Kan, A.A. Azmi, F.S. Yong Julius, P.W. Chia, Green synthesis, characterization and applications of silver nanoparticle mediated by the aqueous extract of red onion peel, Environ. Pollut. 271 (2021) 116295.

[42] Z. Lin, J. Xu, H. Gu, J. Huang, J. Lin, J. Shao, D. Wang, H. Li, A review on research progress in photocatalytic degradation of organic pollutants by Bi_2MoO_6, J. Environ. Chem. Eng. 11 (2023) 110911.

[43] S. Yang, F. Zhang, Y. Shang, L. Luo, Z. Liu, Highly efficient photocatalytic degradation of refractory organic pollutants onto designed boron nitride: morphology control and oxygen doping, J. Clean. Prod. 429 (2023) 139532.

[44] S. Rachmaniar, D.A. Nugraha, D.J.D.H. Santjojo, R.T. Tjahjanto, N. Mufti, Masruroh, prevention of particle agglomeration in sol–gel synthesis of TiO_2 nanoparticles via addition of surfactant, J. Nanopart. Res. 26 (2024) 45.

[45] M.M. Ahmad, S. Mushtaq, H.S. Al Qahtani, A. Sedky, M.W. Alam, Investigation of TiO_2 nanoparticles synthesized by sol-gel method for effectual photodegradation, Oxidation Reduction Reaction, Cryst. 11 (2021) 1456.

[46] A.S. Aliero, N.A. Zawawi, N.A.N.N. Malek, M. Helmi Sani, M.H. Usman, Biogenic synthesis of silver nanoparticles using palm oil mill effluent and its antioxidant potential, Waste Biomass Valor. 16 (2025) 3535–3542.

[47] M.L. Matias, A.S. Reis-Machado, J. Rodrigues, T. Calmeiro, J. Deuermeier, A. Pimentel, E. Fortunato, R. Martins, D. Nunes, Microwave synthesis of visible-light-activated $g\text{-}C_3N_4/TiO_2$ photocatalysts, Nanomater 13 (2023) 1090.

[48] Y. Liu, J. Tian, L. Wei, Q. Wang, C. Wang, C. Yang, A novel microwave-assisted impregnation method with water as the dispersion medium to synthesize modified $g\text{-}C_3N_4/TiO_2$ heterojunction photocatalysts, Opt. Mater. 107 (2020) 110128.

[49] X. Gui, Y. Zhou, Q. Liang, M. Zhou, X. Li, S. Xu, Z. Li, Construction of porous ZnS/TiO_2 S-scheme heterostructure derived from MOF-on-MOF with boosting photocatalytic H_2-generation activity, Int. J. Hydrog. Energy 48 (2023) 38237–38250.

[50] Q. Liang, W. Ma, Y. Shi, Z. Li, X. Yang, Hierarchical Ag_3PO_4 porous microcubes with enhanced photocatalytic properties synthesized with the assistance of trisodium citrate, CrystEngComm 14 (2012) 2966–2973.

[51] R. Feng, M. Guo, Z. Yang, J. Qiu, Z. Wang, Y. Zhao, 0D/2D Bi_2MoO_6 quantum dots /rGO heterojunction boosting full solar spectrum-driven photothermal catalytic CO_2 reduction to solar fuels, Carbon 224 (2024) 119079.

[52] N. Qi, Y. Yi, Y. Tang, X. Liu, Y. Yuan, Z. He, X. Shi, Y. Fang, Y. He, S. Wei, Constructing a novel $Bi_2MoO_6/TiO_2/Ti_3C_2$ composite with efficient carrier separation for excellent photocatalytic purification of TC, J. Alloys Compd. 1010 (2025) 177575.

[53] C. Ruan, W. Wang, Z. Dai, G. Zheng, The enhanced electrons and holes separation for Bi_2MoO_6/TiO_2 Z-scheme heterojunction by Ag loading, J. Wuhan Univ. Technol.-Mat. Sci. Ed. 38 (2023) 996–1002.

[54] X.-P. Wei, Y.-T. Yang, S.-Y. Li, Y. Meng, W.-B. Yuan, H.-G. Ni, Dual role of oxygen vacancies in TiO_2/Bi_2O_3 for enhanced carrier separation and PDS activation: a combined experimental and DFT study, Environ. Res. 282 (2025) 122042.

[55] D. Kanakaraju, F.D. Anak Kutiang, D.N. Joseph, Y.-C. Lim, M. Vincent, Ionic liquid-mediated TiO_2/Ag/CA photocatalyst for enhanced water remediation, J. Environ. Chem. Eng. 12 (2024) 113186.

[56] Z. Yin, S. Qi, S. Deng, K. Xu, Z. Liu, M. Zhang, Z. Sun, Bi_2MoO_6/TiO_2 heterojunction modified with Ag quantum dots: a novel photocatalyst for the efficient degradation of tetracycline hydrochloride, J. Alloys Compd. 888 (2021) 161582.

[57] H. Li, X. Luo, Z. Long, G. Huang, L. Zhu, Plasmonic Ag nanoparticle-loaded n-p $Bi_2O_2CO_3/\alpha\text{-}Bi_2O_3$ heterojunction microtubes with enhanced visible-light-driven photocatalytic activity, Nanomaterials (Basel) 12 (2022).

[58] D. Wang, H. Shen, L. Guo, C. Wang, F. Fu, Y. Liang, Ag/Bi_2MoO_{6}-x with enhanced visible-light-responsive photocatalytic activities via the synergistic effect of surface oxygen vacancies and surface plasmon, Appl. Surf. Sci. 436 (2018) 536–547.

[59] Y. Lu, C. Ding, J. Guo, W. Gan, P. Chen, M. Zhang, Z. Sun, Highly efficient photodegradation of ciprofloxacin by dual Z-scheme Bi_2MoO_6/GQDs/TiO_2 heterojunction photocatalysts: mechanism analysis and pathway exploration, J. Alloys Compd. 924 (2022) 166533.

[60] M. Ahmadi, S.M. Alavi, A. Larimi, Pt–Cu@Bi_2MoO_6/TiO_2 photocatalyst for CO_2 reduction, Inorg. Chem. 62 (2023) 20372–20389.

[61] G. Yan, X. Cao, Q. Zhao, W. Hu, Z. Zhao, H. Shi, Bismuth-based photocatalysts for formaldehyde photodegradation: a review and prospects, Inorg. Chem. Commun. 178 (2025) 114547.

[62] D. Kanakaraju, F.D. Anak Kutiang, Y.C. Lim, P.S. Goh, Recent progress of Ag/TiO_2 photocatalyst for wastewater treatment: doping, co-doping, and green materials functionalization, Appl. Mater. Today 27 (2022) 101500.

[63] F. Kang, G. Sheng, X. Yang, Y. Zhang, Fabrication of two-dimensional Bi_2MoO_6 nanosheet-decorated $Bi_2MoO_6/Bi_4O_5Br_2$ Type II heterojunction and the enhanced photocatalytic degradation of antibiotics, Inorganics (2024) 289.

[64] E.H. Khader, S.A. Muslim, N.M.C. Saady, N.S. Ali, I.K. Salih, T.J. Mohammed, T. M. Albayati, S. Zendehboudi, Recent advances in photocatalytic advanced oxidation processes for organic compound degradation: a review, Desalin. Water Treat. 318 (2024) 100384.

[65] R.M.D.R. Santana, D.C. Napoleão, J.M. Rodriguez-Diaz, R.K.D.M. Gomes, M. G. Silva, V.M.E.D. Lima, A.A.D. Melo Neto, G.M. Vinhas, M.M.M.B. Duarte, Efficient microbial cellulose/Fe_3O_4 nanocomposite for photocatalytic degradation by advanced oxidation process of textile dyes, Chemosphere 326 (2023) 138453.

[66] T.T.H. Duong, S. Ding, M. Sebek, H. Lund, S. Bartling, T. Peppel, T.S. Le, N. Steinfeldt, Effect of Bi_2MoO_6 morphology on adsorption and visible-light-driven degradation of 2,4-Dichlorophenoxyacetic acid, Mol 29 (2024) 3255.

[67] B. Wijaya, D.O.B. Apriandanu, R.M. Surya, Y. Yulizar, N.S. Sambudi, M. Khalil, A. Umar, Synthesis of novel $TiO_2/CeFeO_3$ heterojunction using mugwort (*Artemisia vulgaris*) leaves extracts with enhanced photocatalytic activity under visible light irradiation, Appl. Surf. Sci. Adv. 21 (2024) 100599.

[68] A. Umar, C. Claudia, M. Khalil, R. Bakri, H. Bin Bae, K. Tae-Hwan, D.O. B. Apriandanu, Photocatalytic activity of $CuBi_2O_4$/CuO heterojunction for methylene blue degradation under visible light irradiation, Vacuum 238 (2025) 114246.

[69] Y. Yulizar, I. Abdullah, R.M. Surya, N.L. Alifa, Green synthesis of novel $YMnO_3$-doped TiO_2 for enhanced visible-light- driven photocatalytic degradation of malachite green, J. Environ. Manag. 342 (2023) 118139.

[70] I. Pangestu, D.O.B. Apriandanu, R.M. Surya, S. Chandren, Y. Yulizar, Visible-light response $ZnO/CuCo_2O_4$ nanocomposite: vibrational, optical, structural, morphological, photocatalytic, and kinetic analyses, Ceram. Int. 50 (2024) 34321–34330.

[71] R.D.F. Irbati, D.O.B. Apriandanu, M. Rahayu, V.R. Ananda, M.R. Yusuf, S. Chandren, Y. Yulizar, Green fabrication of novel $LaCeO_3$ decorated with CuO using *Kigelia africana* (lamb) benth leaf extract for photocatalytic degradation of malachite green, Nano-Struct. Nano-Objects 42 (2025) 101474.

[72] R.A. Fernandes, M.J. Sampaio, G. Dražić, J.L. Faria, C.G. Silva, Efficient removal of parabens from real water matrices by a metal-free carbon nitride photocatalyst, Sci. Total Environ. 716 (2020) 135346.

[73] Z.U.H. Khan, N.S. Gul, S. Sabahat, J. Sun, K. Tahir, N.S. Shah, N. Muhammad, A. Rahim, M. Imran, J. Iqbal, T.M. Khan, S. Khasim, U. Farooq, J. Wu, Removal of organic pollutants through hydroxyl radical-based advanced oxidation processes, Ecotoxicol. Environ. Saf. 267 (2023) 115564.

[74] K.J. Berean, E.M. Adetutu, J. Zhen Ou, M. Nour, E.P. Nguyen, D. Paull, J. McLeod, R. Ramanathan, V. Bansal, K. Latham, G.J. Bishop-Hurley, C. McSweeney, A.S. Ball, K. Kalantar-zadeh, A unique in vivo approach for investigating antimicrobial materials utilizing fistulated animals, Sci. Rep. 5 (2015) 11515.

[75] Z. Zhao, W. Zhang, Y. Sun, J. Yu, Y. Zhang, H. Wang, F. Dong, Z. Wu, Bi Cocatalyst/Bi_2MoO_6 microspheres nanohybrid with SPR-promoted visible-light photocatalysis, J. Phys. Chem. C 120 (2016) 11889–11898.

[76] Q. Lang, Y. Chen, T. Huang, L. Yang, S. Zhong, L. Wu, J. Chen, S. Bai, Graphene “bridge” in transferring hot electrons from plasmonic Ag nanocubes to TiO_2 nanosheets for enhanced visible light photocatalytic hydrogen evolution, Appl. Catal. B Environ. 220 (2018) 182–190.

[77] P.T. Le, T.P. Nguyen, H.N. Nguyen, T.H. Tran, T.H. Do, P.T. Thuy, T.M. Thanh Dinh, T. Tsubota, V.D. Nguyen, T.D. Nguyen, Z-scheme $Bi_2MoO_6/g\text{-}C_3N_4$ heterojunction for efficient antibiotic degradation via persulfate activation under visible light, Water Sci. Eng. 18 (2025) 515–526.

[78] S. Vignesh, A.L. Muppudathi, J.K. Sundar, Multifunctional performance of $gC_3N_4\text{-}BiFeO_3\text{-}Cu_2O$ hybrid nanocomposites for magnetic separable photocatalytic and antibacterial activity, J. Mater. Sci. Mater. Electron. 29 (2018) 10784–10801.

[79] X. Ma, H. Wang, Y. Chen, L. Fu, J. Zhou, L. Zhang, Z. Xing, Q. Zhang, L. Xia, Application of Ag@$g\text{-}C_3N_4/TiO_2$ cotton fabric flexible substrate with dual functionality: photocatalytic reusability and SERS signal amplification for food safety detection, Appl. Surf. Sci. 661 (2024) 160068.

[80] S. Anees Ahmad, S. Sachi Das, A. Khatoon, M. Tahir Ansari, M. Afzal, M. Saquib Hasnain, A. Kumar Nayak, Bactericidal activity of silver nanoparticles: a mechanistic review, Mater. Sci. Energy Technol. 3 (2020) 756–769.

[81] K. Chen, X. Feng, R. Hu, Y. Li, K. Xie, Y. Li, H. Gu, Effect of ag nanoparticle size on the photoelectrochemical properties of ag decorated TiO_2 nanotube arrays, J. Alloys Compd. 554 (2013) 72–79.

[82] J. Bahadur, S. Agrawal, V. Panwar, A. Parveen, K. Pal, Antibacterial properties of silver doped TiO_2 nanoparticles synthesized via sol-gel technique, Macromol. Res. 24 (2016) 488–493.

[83] D. Dhanalekshmi, K.S. Meena, I. Ramesh, Synthesis and characterization of Ag@ TiO_2 core-shell nanoparticle and study of its antibacterial property, Int. J. Nanotech. App.3 (2013) 5–14.

[84] S. Hartati, A. Zulfi, P.Y.D. Maulida, A. Yudhowijoyo, M. Dioktyanto, K.E. Saputro, A. Noviyanto, N.T. Rochman, Synthesis of electrospun PAN/TiO_2/Ag nanofibers membrane as potential air filtration media with photocatalytic activity, ACS Omega 7 (2022) 10516–10525.

[85] Y. Xie, X. Wang, H. Li, T. Wang, W. Feng, J. Li, PAN/TiO_2 ultrafiltration membrane for enhanced BSA removal and antifouling performance, Catalysts 13 (2023) 1320.

[86] P. Tshindane, B.B. Mamba, M.M. Motsa, T.T.I. Nkambule, Delayed solvent–nonsolvent demixing preparation and performance of a highly permeable polyethersulfone ultrafiltration membrane, Membranes (2023) 39.

[87] N. Peng, T.-S. Chung, K.Y. Wang, Macrovoid evolution and critical factors to form macrovoid-free hollow fiber membranes, J. Membr. Sci. 318 (2008) 363–372.

[88] T.W. Quadri, O.E. Fayemi, L.O. Olasunkanmi, E.E. Ebenso, Chapter 15 - survey of different electrochemical and analytical techniques for corrosion measurements, in: J. Aslam, C. Verma, C. Mustansar Hussain (Eds.), Electrochemical and Analytical Techniques for Sustainable Corrosion Monitoring, Elsevier, 2023, pp. 293–323.

[89] A. Basko, T. Lebedeva, M. Yurov, A. Ilyasova, G. Elyashevich, V. Lavrentyev, D. Kalmykov, A. Volkov, K. Pochivalov, Mechanism of PVDF membrane formation by NIPS revisited: effect of precipitation bath nature and polymer–solvent affinity, Polymers (2023) 4307.

[90] M. Xiao, X. Wang, Z. Hou, J. Alan Quezada Renteria, D.S. Dlamini, D. Jassby, E.M. V. Hoek, Comparison of classical hydrodynamic models of transport through porous membranes, Sep. Purif. Technol. 360 (2025) 131189.

[91] O. Myronyuk, E. Vanagas, A.M. Rodin, M. Wesolowski, Estimation of the structure of hydrophobic surfaces using the cassie–baxter equation, Materials (2024) 4322.

[92] G.Z. Ramon, E.M.V. Hoek, Transport through composite membranes, part 2: impacts of roughness on permeability and fouling, J. Membr. Sci. 425-426 (2013) 141–148.